# $M_W$ 6.0 KARONGA, MALAWI EARTHQUAKE OCCURRED ON CENOZOIC FAULTS THAT REACTIVATED PRECAMBRIAN SHEAR ZONE: EVIDENCE FROM AEROMAGNETIC AND ELECTRICAL RESISTIVITY IMAGING

By

FOLARIN KOLAWOLE

Bachelor of Science in Applied Geology

Federal University of Technology, Akure (F.U.T.A.)

Akure, Ondo State, Nigeria

2008

Submitted to the Faculty of the
Graduate College of the
Oklahoma State University
in partial fulfillment of
the requirements for
the Degree of
MASTER OF SCIENCE
July, 2017

$M_W$ 6.0 KARONGA, MALAWI EARTHQUAKE OCCURRED ON CENOZOIC FAULTS THAT REACTIVATED PRECAMBRIAN SHEAR ZONE: EVIDENCE FROM AEROMAGNETIC AND ELECTRICAL RESISTIVITY IMAGING

Thesis Approved:

Dr. Estella Atekwana

Thesis Adviser

Dr. Mohamed G. Abdelsalam

Dr. Daniel Laó-Dávila

ACKNOWLEDGMENTS

This research opportunity would not have been possible without my professor, mentor, and committee chair, Dr. Estella Atekwana of Oklahoma State University (OSU). Thank you for countless hours of instruction, motivation and guidance in helping me to become a better geoscientist. I am definitely indebted to you. I am also grateful for my other committee members, Dr. Mohamed Abdelsalam and Dr. Daniel Laó-Dávila for your suggestions and advice in improving my thesis.

Special thanks to the 2015 International Research Experience for Students (IRES) participants B. Clappe, C. Hull, T. Johnson, V. Nyalugwe, and S. Dawson for helping with the acquisition of the resistivity data used in this study. I would like to extend my sincere gratitude to the Geological Survey Department of Malawi for providing the aeromagnetic and earthquake data used for my thesis. This work was partially supported by the National Science Foundation (NSF) grant no. II – 1358150 and NSF-EAR 1255233.

I would like to thank Oklahoma State University and the Boone Pickens School of Geology for providing me with an education that has prepared me for my future. I am grateful for all of the scholarships I have been blessed to earn, especially the Decker Dawson Graduate Fellowship in Geophysics Scholarship, the Skinner Geology Fellowship, and the Boone Pickens School of Geology Student Enrichment Fund awards that assisted me in pursuing my education and presenting my thesis research

at various scientific conferences. Thank you to all of the professors at Boone Pickens School of Geology who have impacted my life in a positive way and have helped me succeed as a graduate student. Special thanks to all the members of the Tectonics Research Group at Boone Pickens School of Geology for proving me a rich, diverse, inclusive, supportive and vibrant scientific environment that enabled me to grow and learn more about the geology of various tectonic settings. I appreciate all of my friends that continued to encourage me and bring joy to my life while attending OSU.

I offer my heartfelt appreciation to my wife, Mrs. Abolore Muraina, for her love, understanding, patience and unwavering support for me and my career throughout the course of my Masters degree program at OSU. I would not have been able to attain this academic feat without your insights, motivation and encouragement.

I also appreciate my brothers and mum in Nigeria for their constant encouragement and support. I want to thank my mum for instilling in me the qualities and characteristics I needed to excel in life. Ultimately. I thank God almighty whose breath and grace had kept me though life's challenges.

Acknowledgements reflect the views of the author and are not endorsed by committee members or Oklahoma State University.

Name: Folarin Kolawole Date of Degree: July, 2017

Institution: Oklahoma State University Location: Stillwater, Oklahoma

Title of Study: $M_W$ 6.0 KARONGA, MALAWI EARTHQUAKE OCCURRED ON CENOZOIC FAULTS THAT REACTIVATED PRECAMBRIAN SHEAR ZONE: EVIDENCE FROM AEROMAGNETIC AND ELECTRICAL RESISTIVITY IMAGING

Pages in Study: 78 Candidate for the Degree of Master of Science

Major Field: Geology

- Surface rupture locations of 2009 Karonga, Malawi earthquake aligns with a distinct magnetic lineament in the basement.
- Electrical resistivity data confirms partial rupture of reactivated basement fault.
- Strain accommodation in Karonga area associated with breaking-up of the hinge zone of the North Basin half graben, modulated by reactivation of Precambrian basement fabric.

Summary: The 2009 Karonga, Malawi earthquake caused a surface rupture length of 14-18 km along a single W-dipping fault on the hanging wall of the North Basin of the Malawi Rift. This part of the rift is underlain by the NW-trending Precambrian Mughese Shear Zone (MSZ). I used aeromagnetic and electrical resistivity data to elucidate the relationship between surface rupture locations and pre-existing structures. Although several magnetic lineaments are visible in the basement, mapped surface ruptures align with a single 37 km-long, 148°-162° - striking magnetic lineament dipping 40°SW, and is characterized by a zone of electrical disturbance associated with near-surface soil liquefaction features. Fault geometries, regional kinematics and spatial distribution of seismicity suggest that seismogenic faults reactivated the basement fabric found along the half-graben hinge zone. I suggest that focusing of strain accommodation and seismicity along the half-graben hinge zone is facilitated and modulated by the presence of the basement fabric.

TABLE OF CONTENTS

Chapter Page

I. ACTIVE DEFORMATION OF MALAWI RIFT'S NORTH BASIN HINGE ZONE MODULATED BY REACTIVATION OF PRE-EXISTING PRECAMBRIAN SHEAR ZONE FABRIC .....1

1. Introduction

2. Recent Earthquakes in Northern Malawi Rift
   2.1. The 2009 Karonga Earthquake Swarm
   2.2. The 2014 Karonga Earthquake Sequence

3. Geological and Tectonic Setting
   3.1. The Malawi Rift
   3.2. The North Basin
   3.3. Pre-Malawi Rift Formations

4. Data and Methods
   4.1. Aeromagnetic data

5. Results
   5.1. Filtered aeromagnetic maps
   5.2. Distribution of earthquake surface ruptures
   5.3. Geological cross-section

6. Discussion
   6.1. Relationship between surface rupture locations and magnetic lineaments
   6.2. Relationship between basement structures and the Mughese Shear Zone (MSZ) fabric
   6.3. Half-graben hinge zone deformation
   6.4. Implications for earthquake hazards

7. Conclusions

Acknowledgements
References

II. ELECTRICAL RESISTIVITY AND TEMPORAL AEROMAGNETIC IMAGING OF THE 2009 KARONGA, MALAWI EARTHQUAKE CAUSATIVE FAULT

AND RUPTURE ZONE .....50

Summary

1. Introduction

2. Geological setting

3. Data and methods
   3.1. Aeromagnetic data
   3.2. Earthquake surface ruptures
   3.3. Electrical resistivity tomography (ERT)

4. Results
   4.1. Filtered aeromagnetic data
   4.2. Distribution of earthquake surface deformation locations
   4.3. ERT data

5. Discussion
   5.1. Origin of the ruptured fault and seismotectonic framework of the Karonga area
   5.2. Near-surface structure of earthquake rupture zone
   5.3. Implications for seismic hazards

6. Conclusions

Acknowledgements
References

# CHAPTER I

# ACTIVE DEFORMATION OF MALAWI RIFT'S NORTH BASIN HINGE ZONE MODULATED BY REACTIVATION OF PRE-EXISTING PRECAMBRIAN SHEAR ZONE FABRIC

F. Kolawole[1], E. A. Atekwana[1], D. A. Laó-Dávila[1], M. G. Abdelsalam[1], T. Ivey[1], P. R. Chindandali[2], J. Salima[2], and L. Kalindikafe[3]

[1]Oklahoma State University Main Campus, Stillwater, OK 74078, United States

[2]Geological Survey Department of Malawi, P.O. Box 27, Zomba, Malawi

[3]Malawi University of Science and Technology, P.O. Box 5196, Limbe, Malawi

Corresponding author: Estella Atekwana (estella.atekwana@okstate.edu)

Key Points:

1. We used aeromagnetic data to elucidate the relationship between the locations of the 2009 Mw 6.0 Karonga, Malawi earthquake surface ruptures and buried faults.
2. Surface rupture locations align with a distinct magnetic lineament in the basement.
3. Seismicity and strain accommodation in the North Basin hinge zone is modulated by reactivation of the underlying Precambrian shear zone fabric.

**Abstract**

We integrated temporal aeromagnetic data and recent earthquake data to address the long-standing question on the role of pre-existing Precambrian structures (here referred to as basement fabric) in modulating strain accommodation and subsequent ruptures leading to seismic events within the East African Rift System (EARS). We used aeromagnetic data to elucidate the relationship between the locations of the 2009 $M_w$ 6.0 Karonga, Malawi earthquake surface ruptures and buried basement faults along the hinge zone of the half-graben comprising the North Basin of the Malawi Rift (here referred to as half-graben hinge zone). Through the application of derivative filters and depth-to-magnetic-source modeling, we identified and constrained the trend of the Precambrian metamorphic fabrics at the rift flanks and beneath the basin sedimentary cover, and correlated them to the three-dimensional (3D) structure of buried basement faults. Our results reveal an unprecedented detail of the basement fabric dominated by high frequency WNW- to NW-trending magnetic lineaments associated with the Precambrian Mughese Shear Zone fabric. These are superimposed by lower frequency NNW-trending magnetic lineaments associated with possibly Cenozoic faults in areas overlain by rift sedimentary rocks. Surface ruptures associated with the 2009 $M_w$ 6.0 Karonga earthquake swarm aligned with one of the NNW-trending magnetic lineaments defining a normal fault that is characterized by right-stepping segments along its northern half and coalesced segments on its southern half. Fault geometries, regional kinematics and spatial distribution of seismicity suggest that seismogenic faults reactivated the basement fabric found along the half-graben hinge zone.

We suggest that focusing of strain accommodation and seismicity along the half-graben hinge zone is facilitated and modulated by the presence of the basement fabric.

Index Terms: 8010 Fractures and faults, 8004 Dynamics and mechanics of faulting, 8025 Mesoscopic fabrics, 8002 Continental neotectonics (8107), 8109 Continental tectonics: extensional (0905), 9305 Africa, 0925 Magnetic and electrical methods (5109), 7230 Seismicity and tectonics (1207, 1217, 1240, 1242).

Keywords: Malawi Rift, North Basin, Karonga Basin, 2009 Karonga Earthquake, Shear zone, Reactivation, Pre-existing structures, Normal fault

## 1. Introduction

The contributions of faulting and magmatism to strain accommodation within weakly extended, magma-poor youthful continental rifts remain poorly-understood as there are limited locations worldwide where these processes can be actively documented. The East African Rift System (EARS; Figure 1a) is the largest seismically-active rift system on Earth in which deep seismicity is localized along or near major border faults, while relatively shallower seismicity is mostly associated with strain localization within the rift axis [*Kearey et al*., 2009; *Craig et al*., 2011]. Absence of basin-ward migration of faulting and an overall extension localization on faults established in the early stage of rifting has been observed in a part of the EARS [*McCartney and Scholz*, 2016]. However, numerous studies

have shown that extension in the early stage of rifting is accommodated by displacement along border faults. As rifts evolve, extension is transferred to the hanging-wall, often facilitated by diking and magma intrusion [e.g. *Ebinger and Casey*, 2001; *Goldsworthy and Jackson*, 2001; *Wright et al*., 2006; *Calais et al*., 2008]. It has been shown that the localization of brittle deformation within the border fault hanging-wall is not entirely controlled by the flexure of the hanging-wall, but can be assisted by intrusion and release of magmatic volatiles into the hanging-wall [*Muirhead et al*., 2016]. Located within the southern segment of the EARS, the North Basin of the Malawi Rift (Figure 1b) is a rift in which basin-ward migration of tectonic activity has been proposed [*Biggs et al.*, 2010].

On a continental scale, studies have documented the influence of pre-existing structures associated with Precambrian orogenic belts in facilitating localization of extension during the initiation of rifting in different segments of the EARS [*Versfelt and Rosendahl*, 1989; *Wheeler and Karson*, 1989; *Ring*, 1994; *Modisi et al*., 2000; *Kinabo et al*., 2007; 2008; *Katumwehe et al.*, 2015; *Leseane et al.*, 2015]. On a basin scale, studies have also highlighted the role of pre-existing structures in determining the compartmentalization and internal structural architecture of individual rift basins [e.g., *Mortimer et al.*, 2016a; *Phillips et al*., 2016]. Most studies that investigated the influence of pre-existing metamorphic basement structures (here referred to as basement fabric) on rift development relied on kinematic analysis of geologic field data [e.g. *Ring*, 1994; *Beacom et al.*, 2001; *Ring et al.*, 2005], interpretation of remote sensing data [e.g., *Laó-Dávila et al*., 2015], interpretation of two-dimensional (2-D) crustal-scale active-source

seismic data [e.g. *Wilson et al.*, 2010], three-dimensional (3-D) active-source seismic data [e.g. *Phillips et al*., 2016], fault plane solutions from passive seismic data [e.g. *Hussein et al.*, 2006], and numerical and analogue modeling [e.g., *Morley et al*., 2004; *Corti et al.*, 2007]. While these approaches produced significant results, recent work also highlighted the importance of high resolution aeromagnetic data in understanding the complexity of the influence of basement fabric in the evolution of continental rifts including their nucleation, segmentation, and termination [e.g., *Katumwehe et al*., 2015]. Further, the role of basement fabric in modulating intraplate seismicity has been observed in segments of the Precambrian structures in eastern Africa. For example, earthquakes in South Sudan have been associated with reactivation of the Precambrian Aswa Shear Zone [Figure 1a; *Moussa, 2008*]. Nonetheless, the continual role of basement fabric in shaping the architecture of rift systems and subsequent ruptures leading to seismic events has not been fully understood.

The EARS, especially its Western Branch, is predominantly made-up of half-graben basins linked by step-over transfer zones [e.g., *Rosendahl*, 1987; *Chorowicz*, 2005]. The half-grabens are typically 20-50 km wide with hanging-wall blocks deformed by normal faults that are both synthetic and antithetic to a single master border fault [e.g., *Rosendahl et al.*, 1986; *Rosendahl*, 1987; *Bott*, 1997]. The architecture of a half-graben typically consists of a border fault zone, the hanging-wall zone and the hinge zone [Figures 1c and d; e.g., *Rosendahl et al.*, 1986; *Morley*, 1995; *McCartney and Scholz*, 2016]. The border fault zone refers to the region around the deepest side of the half-graben, where

depocenters containing up to several kilometers of sediment thickness lie adjacent to the master border fault [e.g., *Wheeler and Karson*, 1989; *Withjack et al.*, 2002]. The hanging-wall zone represents the rift floor which lies between the border fault zone and the hinge zone. The hinge zone is the area of greatest curvature in the hanging-wall, which is commonly assumed to have developed passively as a result of crustal flexure in response to vertical displacements along the master border fault.

In this study, we show that the distribution of brittle strain along the hinge zones of weakly extended magma-poor half grabens is not entirely caused by crustal flexure, but can be facilitated and modulated by basement fabric. The recent 2009 Karonga earthquake swarm and the 2014 Karonga earthquake sequence in northern Malawi Rift, a sign of active deformation, were localized along the hinge zone of the half-graben comprising the North Basin of the Malawi Rift (here referred to as half-graben hinge zone) [Figures 1b and 2; *Biggs et al.*, 2010; *Oliva et al.*, 2016]. These seismic events allow us to address the persistent question of whether and how basement fabric modulate strain accommodation and seismicity in weakly extended, magma-poor continental rifts. Although there is lack of subsurface data (e.g. in the form of seismic data; Figure 2 Inset) along the half-graben hinge zone, the availability of temporal aeromagnetic data and their effectiveness in imaging basement fabric and basement faults provide an unprecedented view of the geological architecture of the half-graben hinge zone.

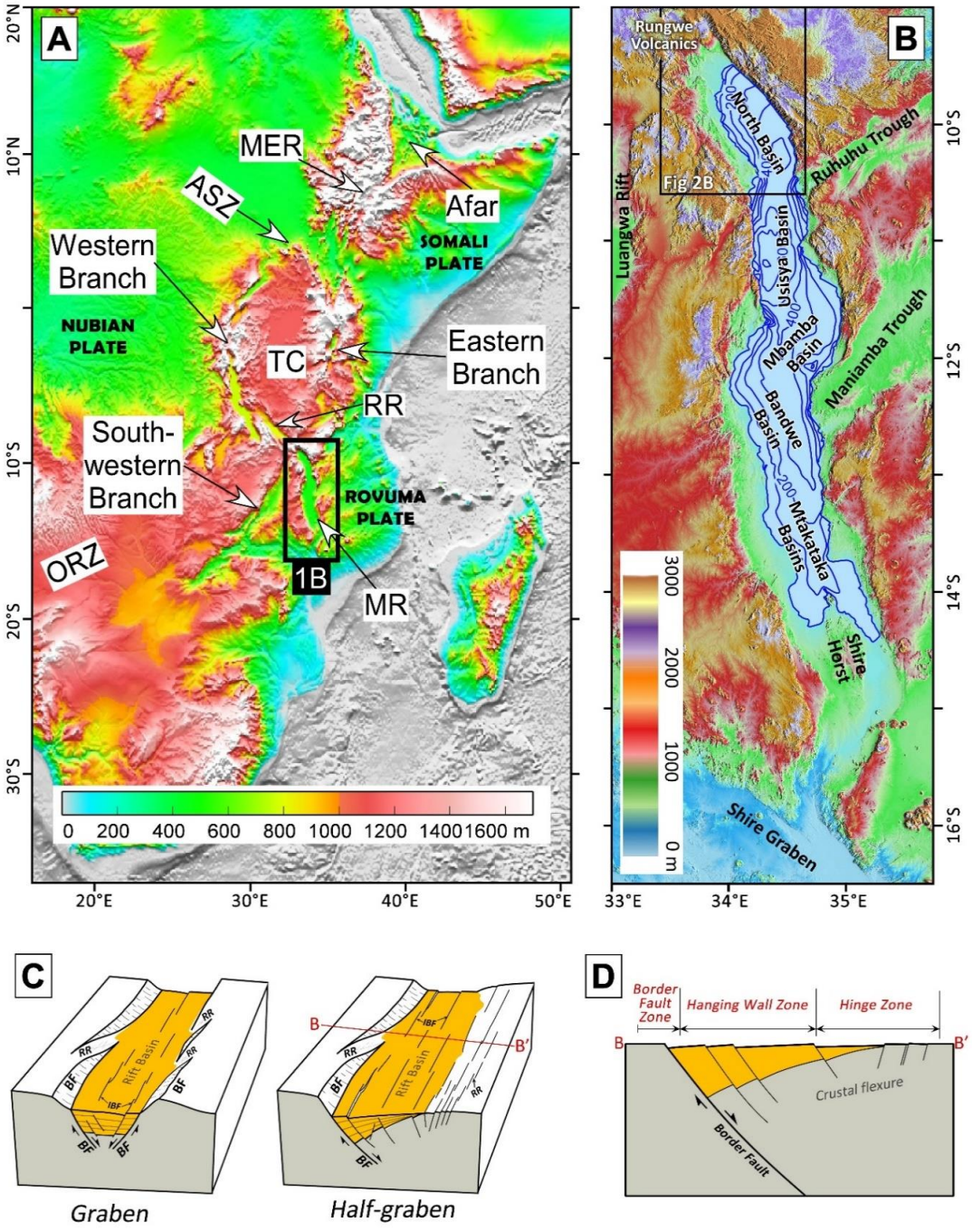


**Figure 1.** (a) Shuttle Radar Topography Mission (SRTM) Digital Elevation Model (DEM) of eastern Africa, showing the location of the Malawi Rift (MR) within the East African Rift System (EARS). ASZ = Aswa Shear Zone, MER = Main Ethiopian Rift, ORZ =

Okavango Rift Zone, RR = Rukwa Rift, TC = Tanzania Craton. (b) SRTM DEM showing different segments of the Malawi Rift. (c) Schematic diagrams of a graben and half-graben. BF = Border fault, IBF = Intrabasin fault, RR = Relay ramp. (d) Schematic diagram of a cross-section across a half-graben, showing the overall structural architecture of a typical half-graben.

We use derivative filters to enhance the magnetic anomalies of the basement fabric and faults which revealed the detailed geometry of the Precambrian Mughese Shear Zone (MSZ) and younger faults, possibly Cenozoic in age. We determine the spatial correlation between basement fabric, basement faults and the locations of the 2009 Karonga earthquake surface ruptures in order to assess the role of basement fabric in facilitating fault ruptures that trigger moderate magnitude earthquakes. Here, we show that the deformation of the half-graben hinge zone is actively modulated by reactivation of the basement fabric.

## 2. Recent Earthquakes in Northern Malawi Rift

### 2.1. The 2009 Karonga Earthquake Swarm

The Karonga area, located in the North Basin of the Malawi Rift was affected by multiple episodes of $M_w$ 4.9 – 6.0 earthquakes between December 6 and 19, 2009 (Figure 2). The series of earthquakes damaged thousands of houses and resulted in several fatalities [*Biggs et al*., 2010]. Additional series of $M_b \leq 4.6$ earthquakes were recorded until one month after the larger events [*Hamiel et al*., 2012].

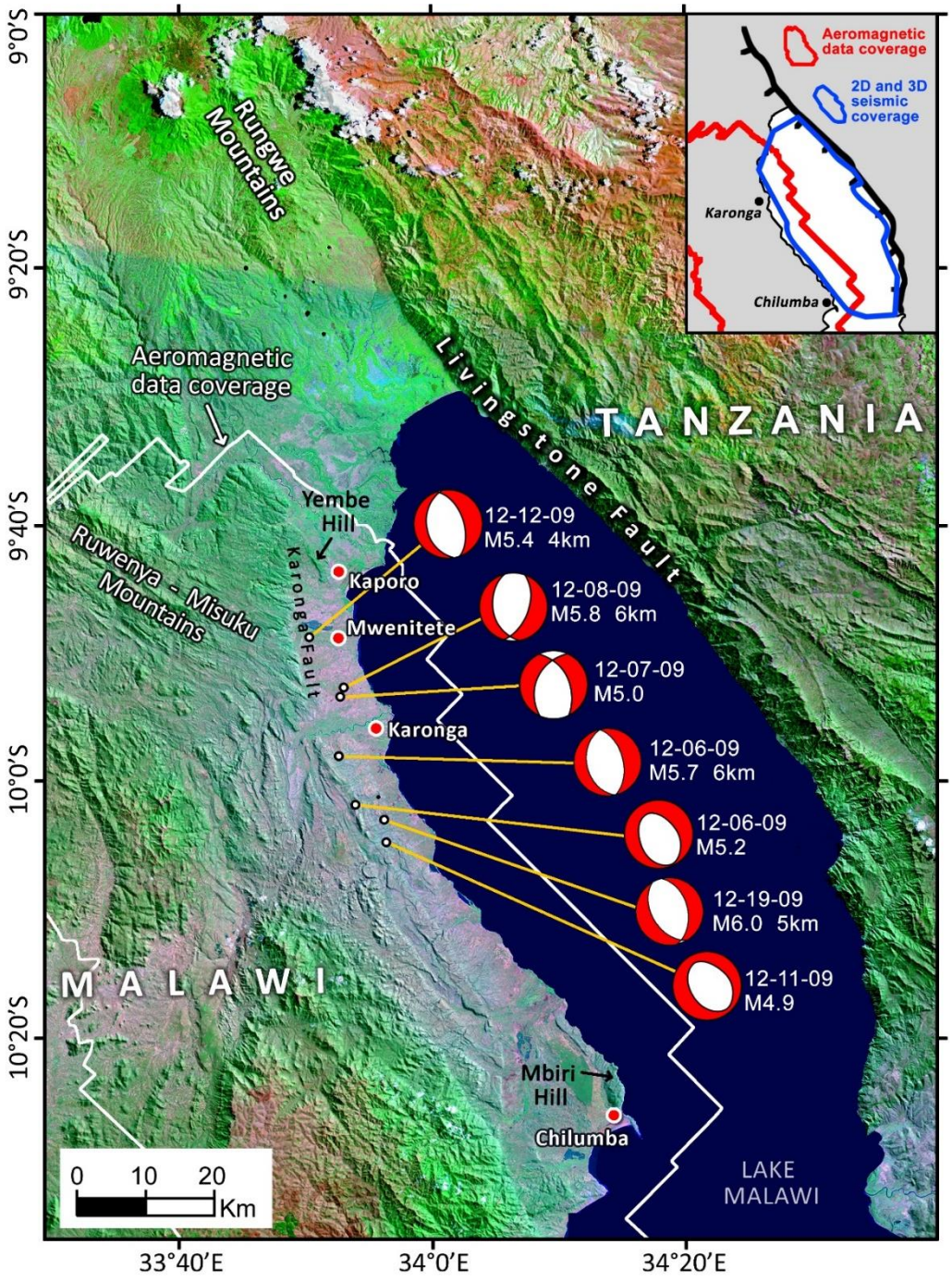


**Figure 2.** 742 (Red-Green-Blue) Landsat Thematic Mapper (TM) image draped onto Shuttle Radar Topography Mission (SRTM) Digital Elevation Model (DEM) of northern Malawi showing major rift-related morpho-tectonic features and location of fault plane

solutions and centroid depths of $M_w \geq 4.9$ earthquakes associated with the December 2009 Karonga earthquake swarm. The earthquake data are from *Biggs et al.* [2010] and Global Centroid Moment Tensor database. White solid open polygon represents the area covered by aeromagnetic data in Figures 4 and 5. **Inset:** map of the North Basin showing the aerial coverage of previously published seismic data [blue polygon; *Mortimer et al*., 2007] relative to aeromagnetic data coverage (red polygon; this study).

The $M_w \geq 4.9$ earthquakes, occurring at <10 km focal depths, were accompanied by coseismic surface ruptures of 35 - 43 cm vertical displacements [*Hamiel et al*., 2012; *Macheyeki et al.,* 2015] and liquefaction-related sand blows within the surficial coastal plain sediments. Differential Interferometric Synthetic Aperture Radar (DInSAR) modeling of the surface deformation associated with the coseismic events suggest that the earthquakes were not associated with magmatic emplacement [*Biggs et al*., 2010]. Instead, these studies found that the earthquake sequence was associated with the rupture of a shallow single NNW-SSE striking and SW-dipping normal fault [*Biggs et al.*, 2010; *Hamiel et al*., 2012; *Macheyeki et al.*, 2015] associated with active deformation of the half-graben hinge zone. *Hamiel et al.* [2012] documented a cumulative surface rupture length of 18 km, while *Macheyeki et al*. [2015] estimated a total rupture length of 14.3 km. *Macheyeki et al.* [2015] suggested that the fault that ruptured during the earthquake has three segments with observed ~1.6 km-long along-strike separation between them. Since the ruptured fault had no known surface expression before the earthquake swarm, its origin is unknown. It is also not clear if the rupture created a new fault or occurred on a pre-existing fault.

### 2.2. The 2014 Karonga Earthquake Sequence

Between December 31, 2014 and January 1, 2015, three $M_w$ 5.1 seismic events were recorded by the SEGMeNT (Study of Extension and maGmatism in Malawi aNd Tanzania) array [*Oliva et al.,* 2016]. The earthquake epicenters were located within the Mwenitete-Kaporo area (~15 km north of Karonga town, Figure 2), with hypocentral locations at 5-10 km depths. The fault plane solutions for the earthquake sequence suggest normal faulting on N-S and NNW –striking planes.

## 3. Geological and Tectonic Setting

### 3.1. The Malawi Rift

The magma-poor Malawi Rift can be divided into three segments [Figure 1b; *Carter and Bennett*, 1973; *Ebinger et al.*, 1989; *Ring*, 1994; *Laó-Dávila et al.*, 2015]: (1) The northern segment that consists of the North Basin (also known as the Karonga Basin), the Usisya Basin, Mbamba Basin and the Bandwe Basin. The North Basin has a SW-dipping border fault and the basin is tilted to the northeast. The Usisya Basin has an E-dipping border fault and the basin tilts to the west. The Mbamba Basin has a W-dipping border fault and the basin tilts to the east, and the Bandwe Basin has an E-dipping border fault while the basin tilts to the west. (2) The central segment consisting of the Metangula and Mtakataka Basins have poorly-developed border faults that are mostly W-dipping faults. Both basins are tilted to the east. (3) The southern segment of the rift consists of a bifurcated and southward-shallowing graben system that terminates at the WNW-ESE -trending Shire Graben.

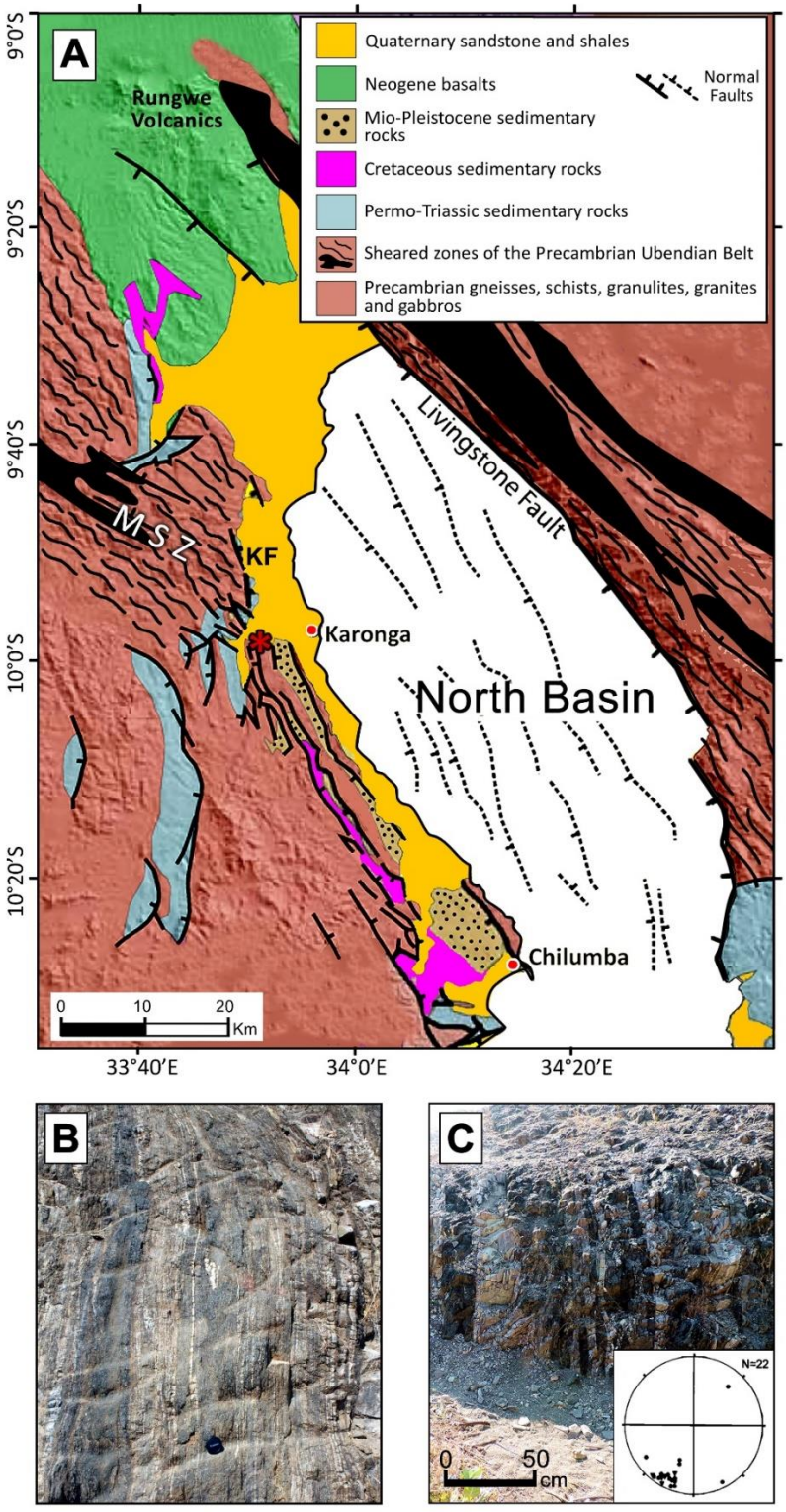
A
Quaternary sandstone and shales
Neogene basalts
Mio-Pleistocene sedimentary rocks
Cretaceous sedimentary rocks
Permo-Triassic sedimentary rocks
Sheared zones of the Precambrian Ubendian Belt
Precambrian gneisses, schists, granulites, granites and gabbros
Normal Faults
Rungwe Volcanics
Livingstone Fault
M S Z
KF
Karonga
North Basin
Chilumba
0 10 20 Km
9°0'S
9°20'S
9°40'S
10°0'S
10°20'S
33°40'E
34°0'E
34°20'E
B
C
N=22
0 50 cm

**Figure 3.** (a) Geological map of the North Basin of the Malawi Rift modified after *Wheeler and Karson* [1989] and *Biggs et al.* [2010]. MSZ = Mughese Shear Zone (Precambrian), KF = Karonga fault. (b and c**)** Field photographs of the basement fabric in the outcrops of the MSZ at a location ~10 km west of Karonga town, along M26 road (red asterisk in Figure 3a). Figure C inset is a stereonet [from *Ring*, 1994] showing orientation and steep dips of foliation and minor shear zones within the MSZ.

### 3.2. The North Basin

The North Basin is a typical half-graben, bound on the east by the 100 km-long, NW-striking and steeply (60°) SW-dipping Livingstone Fault [*Wheeler and Karson*, 1989; *Mortimer et al.*, 2016b; Figures 2 and 3a]. The hanging-wall block of the fault has been deformed by numerous NW-striking ~55°-dipping intra-basin normal faults found under Lake Malawi [*Mortimer et al*., 2007]. Most of these intra-basin normal faults are synthetic to the Livingstone Fault [*Ring*, 1994; *Mortimer et al*., 2007]. The North Basin is filled with Neogene-Quaternary Chiwondo and Chitimwe lacustrine sedimentary rocks, which in turn are covered by coastal plain alluvial sediments [*Schrenk et al*., 1993; *Ring*, 1994]. The Quaternary alluvial sediments are composed of sandy clays, terrace sands and gravels [*Macheyeki et al*., 2015].

The kinematic history of the North Basin has been attributed to an initial ENE-WSW directed orthogonal extension during which the development and segmentation of the Livingstone border fault occurred, as well as the development of NW-trending normal faults within the basin [*Ring*, 1994; *Mortimer et al*., 2007]. At 500-400 Ka, tectonic extension rotated into a WNW-ESE direction, such that former intra-basin dip-slip faults

were reactivated as oblique dextral strike-slip faults and associated flower structures [*Ring*, 1994; *Mortimer et al*., 2007]. The Livingstone Fault, which borders the North Basin in the east (Figures 2 and 3a), originated as a reactivation of Precambrian ductile shear zones within the Ubendian Belt, and has accommodated at least 4 km of vertical displacement [*Wheeler and Karson*, 1989]. On the half-graben hinge zone, the Precambrian rocks of the MSZ are truncated by the N-S -trending and E-dipping Karonga Fault, juxtaposing the Precambrian rocks against the Mesozoic and Cenozoic sedimentary rocks of the basin. The Karonga Fault, which is one of the most dominant morpho-structural features on the half-graben hinge zone [*Laó-Dávila et al*., 2015] bounds outcrops of Late Carboniferous - Early Jurassic sedimentary rocks, suggesting that the fault predates Cenozoic rifting in northern Malawi. Using Global Positioning System (GPS), earthquake slip vectors and a rigid plate model, *Stamps et al.* [2008] estimated a rift opening rate of 3.8 mm/year, while *Saria et al.* [2014] estimated 2.2 mm/year, and an E-W present-day tectonic extension direction for the North Basin of the Malawi Rift.

### 3.3. Pre-Malawi Rift Formations

The North Basin is underlain by Paleoproterozoic amphibolite, grey gneisses and granites formed during the Ubendian Orogeny (1,600 Ma) [*Ring et al*., 2002], which were later deformed by the ~30-50 km-wide NW-trending MSZ in the Neoproterozoic (Figure 3a). The shear zone separates the Ubendian orogenic belt in the northeast from the Mesoproterozoic - Neoproterozoic Irumide orogenic belt to the southwest [*Ring*, 1994;

*Fritz et al.*, 2013]. The shear zone developed during the Neoproterozoic - Early Paleozoic Pan African Orogeny (550±100 Ma) in which crustal shortening along the southern boundary of the Ubendian Belt produced sub-vertical sinistral shear zones with the formation of well-developed fabric that were distributed throughout the crust [*Ring et al.*, 2002]. The shear zone is characterized by steeply-dipping (60°-85°) mylonitic fabric (Figures 3b and c; Figure 3c inset) that contains prominent stretching lineation. The shear zone is also characterized by the presence of shear zone-parallel isoclinal intrafolial folds overprinting earlier structures in the Paleoproterozoic rocks [*Ring*, 1993; *Ring et al.*, 2002].

Patches of Late Carboniferous - Early Jurassic Karoo sedimentary rocks outcrop onshore along the Karonga Fault in the western part of the half-graben hinge zone (Figure 3a). The Karoo sedimentary rocks are composed of volcano-sedimentary successions deposited within NE- to NNE and N-trending grabens, and these are intruded by NE-striking doleritic dikes. The regional extension direction during the Karoo is controversial. Based on the fault trends within the Zambezi Rift (south of Malawi Rift), an ENE-WSW directed extension has been inferred [*Daly et al*., 1989]; while a NW-SE directed extension due to the dominant NE to NNE strike of the Karoo rifts and associated doleritic dikes has also been suggested [*Castaing*, 1991]. In the Early Cretaceous, NE-directed extension in the North Basin area resulted in the deposition of fossiliferous red, fluviatile sandstone and siltstones referred to as the ‘Dinosaur Beds’ [*Jacobs et al*., 1990; *Ring*, 1994].

## 4. Data and Methods

In this study, we analyzed pre- and post-earthquake aeromagnetic data, spatial location of surface ruptures and sand blows (both here referred to as surface ruptures), and earthquake epicenter locations. A total of 396 surface rupture location coordinates [*Macheyeki et al*., 2015] and eight (8) surface rupture locations [*Hamiel et al*. [2012] along with 229 epicenter location coordinates of earthquakes associated with the 2009 Karonga earthquake swarm [*Seismological Bulletin of Malawi*, 2015] were used in this study.

### 4.1. Aeromagnetic data

The pre-earthquake aeromagnetic data covering the half-graben hinge zone used in this study was acquired in 1984-1985, with 120 m flight elevation along NE–SW lines with spacing of 1 km and a tie-line spacing of 10 km. The post-earthquake aeromagnetic data used in this study was acquired in 2013 with a flight elevation of 80 m along NE–SW lines with spacing of 250 m. The tie lines were oriented NW–SE and spaced 5 km apart. The pre- and post- earthquake residual magnetic field data were first reduced to the magnetic pole (RTP) [*Baranov*, 1957; *Arkani-Hamed*, 1988] in order to remove the skewness of the anomalies and correctly position magnetic anomalies directly over their sources, thereby making it possible to correlate the anomalies with geological information. To compare the pre- and post-earthquake aeromagnetic maps, we upward-continued the 2013 map to 120 m (flight elevation of the 1984-1985 map), however, due to the difference in line spacing, the 2013 data has a higher resolution (62.5 m) than the 1984-1985 data (250 m). Edge-

enhancement directional filters such as the horizontal gradient magnitude (HG), vertical (Dz) and tilt derivative filters were applied to the RTP aeromagnetic grids in order to enhance shallow subsurface anomalies and highlight structural features [*Ma et al*., 2012]. In order to better delineate faults that have surficial expression in the study area, we draped the filtered aeromagnetic maps on hillshade topographic map of 90 m spatial resolution Shuttle Radar Topography (SRTM) Digital Elevation Model (DEM) (Figure 4). Since there is no report of volcanic sediments or information on remanent magnetization along the half-graben hinge zone, we assume that magnetization within the study area is largely by induction and that the crystalline basement is the dominant magnetic source.

According to *Miller and Singh* [1994] and *Salem et al.* [2007], the first order vertical derivative, first order horizontal gradient and tilt derivative of the RTP aeromagnetic grid enhance the magnetic signatures of shallow crustal structures. Total horizontal derivative (horizontal gradient magnitude) estimates the rate of change of total magnetic intensity in the horizontal-X and horizontal-Y directions. The horizontal-X derivative (Dx) operator estimates the rate of change of total magnetic intensity in the E-W direction, thus enhancing structures that are oriented N-S or sub-parallel to the N-S. The horizontal-Y derivative (Dy) operator estimates the rate of change of total magnetic intensity in the N-S direction, thus enhancing structures that are oriented E-W or sub-parallel to the E-W. The tilt derivative is essentially a ratio of the vertical derivative to the total horizontal derivative, thus estimating the magnitude of the overall rate of change of total magnetic intensity (in all directions). The tilt derivative is one of the most effective

edge-detection filters because it normalizes all the edges in a dataset, such that edges that are subtle and less evident in the horizontal and vertical derivative maps are well enhanced in the tilt derivative map. Since magnetic lineaments representing faults are well imaged on vertical and tilt derivative maps [*Kinabo et al.*, 2007; 2008] vertical and tilt derivative maps, we delineate the variations in the along-strike geometry of magnetic lineaments that represent faults by applying Dx and Dy directional derivative filters on vertical and tilt derivative maps depending on the orientation of the target faults.

*Grauch and Hudson* [2007; 2011] presented simple models describing the various magnetic expressions of normal faults that juxtaposes bodies of contrasting magnetic susceptibilities against one another. In this paper, we interpret basement-rooted normal faults along the half-graben hinge zone in terms of the *Grauch and Hudson* [2007; 2011] thin-thick layers variation-2 model, which shows that a normal fault juxtaposing a highly-magnetized basement against an overlying material of lower magnetic susceptibility is characterized by a magnetic-high anomaly above the footwall and a magnetic-low above the hanging wall. Although it is difficult to determine the sense of displacement and amount of fault throw from aeromagnetic anomalies [*Grauch and Hudson*, 2007], this model shows that the magnetic anomaly (RTP-TMI) above the fault is steepest in the direction of fault dip, and that buried faults are typically characterized by double-peak horizontal gradient magnitude.

We delineate the edges of buried basement faults by the zero-degree tilt derivative contour [*Salem et al.*, 2007]. We also estimated depths to the top of the magnetic sources

(i.e. basement) using the Source Parameter Imaging (SPI) method [*Smith et al.*, 1998; *Smith and Salem*, 2005]. Depth calculations from aeromagnetic data have an accuracy of ±20% [*Gay,* 2009]. Our basement depth estimates at the edge of buried structures were also consistent with estimates from the tilt-depth method of *Salem et al.* [2007]. We estimated the dip angle of the earthquake ruptured fault from the angular relationship between the locations of the 0° tilt at the basement level (at depth) and the coseismic fault ruptures at the ground surface and compare our result with previously published estimates from *Biggs et al.* [2010] and *Hamiel et al.* [2012]. We produce a 2-D aeromagnetic geological section from the depth-to-basement analysis of the 2013 high resolution magnetic data using the SPI technique, tilt derivative, and surface topography estimates from the Near-Global 1-arcsecond SRTM-DEM data (30 m spatial resolution). For areas with thick sedimentary cover, we subset the aeromagnetic map within such areas (ensuring that large magnetic anomalies are not included in the subset) and applied the tilt and directional derivative filters in order to enhance the signals of subtle basement fabric obscured by the thick sedimentary cover and presence of large magnetic anomalies in the vicinity.

## 5. Results

### 5.1. Filtered aeromagnetic maps

The first order directional derivatives of the 1984-1985 and 2013 RTP aeromagnetic data reveal details of the crystalline basement fabric related to the MSZ which are represented by high frequency, short wavelength WNW-NW-trending lineaments of high and low

magnetic gradients, especially apparent northwest and southwest of Karonga town ('MSZ' in Figures 4, 5a and b). However, around Karonga town, the high frequency aeromagnetic lineaments are obscured by lower frequency, longer wavelength NNW-trending magnetic lineaments representing basement normal faults and associated asymmetrical grabens and half-grabens (Figure 4). One of these structures is clearly apparent north of Karonga town bounded in the west by the Karonga Fault (labeled KF in Figure 4). Northwest of Karonga town, within the Ruwenya-Misuku Mountains, the high frequency magnetic fabric defines a WNW-trending (125°) ~22 km-wide zone, that is truncated by a N-S trending curvilinear magnetic feature associated with the Karonga Fault (KF in Figure 4). The second set of magnetic lineaments, which are characterized by lower frequency and longer wavelength anomalies, is superimposed on the MSZ-related magnetic lineaments and are interpreted to represent buried basement-rooted normal faults bounding asymmetrical grabens and half-grabens filled with sedimentary rocks.

In Figure 6a-f, we show various characteristics of the buried faults in Karonga area as enhanced by different derivative filters. The RTP Total Magnetic Intensity (RTP-TMI) map (Figure 6a) shows the long wavelength, low frequency character of the buried faults (KPF, SMF, KTF and LF) and short wavelength, high frequency of the MSZ-related magnetic lineaments. The horizontal-X derivative (Dx) of the RTP-TMI map shows the overall geometry of the ~N-S -striking magnetic lineaments in the area (Figure 6b) whereas the horizontal-Y derivative (Dy) reveals the discontinuities along-strike of each of the ~N-S striking lineaments (i.e. segmentation of the lineaments). The horizontal gradient

magnitude (HG) shows the double-peak anomaly over the faults (Figure 6d) that is characteristic of buried normal faults [*Grauch and Hudson*, 2007]. The vertical derivative (Dz) map also clearly reveals the geometry of the magnetic lineaments representing the faults (Figure 6f), and the tilt derivative shows the geometry of the edge of the faults (0° tilt contour; Figure 6e). From these filtered aeromagnetic maps, we find five major normal faults buried beneath rift sediments along the half-graben hinge zone and these are named St. Mary Fault (SMF), Lupaso Fault (LF), Katesula Fault (KTF), Kaporo Fault (KPF) and Mbiri Fault (MF) (Figures 4, 5a and b, 6a-f and 7a and b). The LF and KTF extend in a northwest direction for ~19 km, SMF for 37 km and KPF for 36 km. The SMF, LF, KTF and MF are within the coastal plain sediments whereas the KPF is offshore beneath Lake Malawi (Figure 4). The 62 km-long MF, for the most part is buried beneath the coastal plain sediments but outcrops in the Chilumba town where it bounds the Mbiri Hill in the west. Only the northernmost segment of the SMF outcrops west of Kaporo town where it bounds the Yembe Hill in the west (Figure 4).

Within the basin fill on the hanging walls of the SMF and KPF, we observe low amplitude, high frequency, short wavelength magnetic lineaments enhanced on the tilt derivative map due to the normalizing effect of the tilt derivative operator (Figure 8a; white arrows in Figure 8b). In order to further enhance the edges associated with these ‘suppressed’ lineaments (low amplitude) and better observe their geometrical trends, we first subset out the tilt derivative grid covering the target area, ensuring that we avoid the higher amplitude anomalies associated with exposed basement rocks (areas west of

Karonga Fault) and buried basement-rooted normal faults (KPF, LF, KTF and the southern segment of the SMF). Horizontal-X, Horizontal-Y and horizontal directional gradient (HDG) filtering of the subset grid revealed the overall geometry of the lineaments (Figures 8c-f). The horizontal-Y derivative filtering of the subset grid enhanced the ~E-W striking segments of the suppressed lineaments (Figure 8e), and horizontal-X derivative of the grid enhanced the associated ~N-S striking segments of the lineaments (Figure 8f). However, a 45° horizontal directional gradient (HDG) filtering of the subset grid (Figure 8d) enhanced all the segments of the suppressed lineaments. We observe that a few of the enhanced lineaments (short lineaments) appear to be unstable in the Dx and Dy derivative maps such that they change orientation depending on the filter used; nevertheless, the longer, more distinct lineaments appear to have the same geometry and orientation in all the maps (lineaments at which white arrows point in Figure 8b). We observe that the MSZ magnetic lineaments strike WNW (125°) northwest of Karonga town, but gradually rotates into a NNW (149°) strike northeast and east of the town (Figure 8d-f). These filtered maps, thus, reveal that the 'suppressed' lineaments align with the NW-trending MSZ magnetic fabric in the exposed basement northwest of Karonga town ("exposed basement" in Figure 8c). In addition, the overall trend of the enhanced 'suppressed lineaments' to north and east of Karonga town is consistent with the trend of the magnetic lineaments of the MSZ outcrops southwest of the Karonga town ("exposed basement" in Figure 8c). These evidences suggest that the 'suppressed' magnetic lineaments represent the continuation of the trend of the MSZ-related magnetic lineaments in the basement beneath the asymmetrical grabens

and half-grabens. South of the Karonga area and all the way to the Chilumba town, the MSZ-related magnetic lineaments change to NW (135°) trend (shown by white arrows in Figure 5a and b).

Figure 8 illustrates the detailed along-strike characteristics of some of the identified basement-rooted normal faults, revealed by the application of horizontal-X derivative (Dx) filter to the vertical derivative of the 2013 aeromagnetic data since the faults generally strike N-S. The segmentation of the northern segment of the SMF is inferred from the horizontal-Y derivative (Dy) and tilt derivative (dotted black line in Figure 6c and black arrows in Figure 6f).

### 5.2. Distribution of earthquake surface ruptures

A plot of the locations of the 2009 Karonga earthquake surface ruptures indicates an NNW-trending zone which extend over a total length of 16.4 km (Figure 7a and b). The mapped surface rupture locations follow the SMF magnetic lineament; however, the surface ruptures only cover about half the length of the lineament. The SMF magnetic lineament is clearly observable on both the 1984-1985 and 2013 aeromagnetic data.

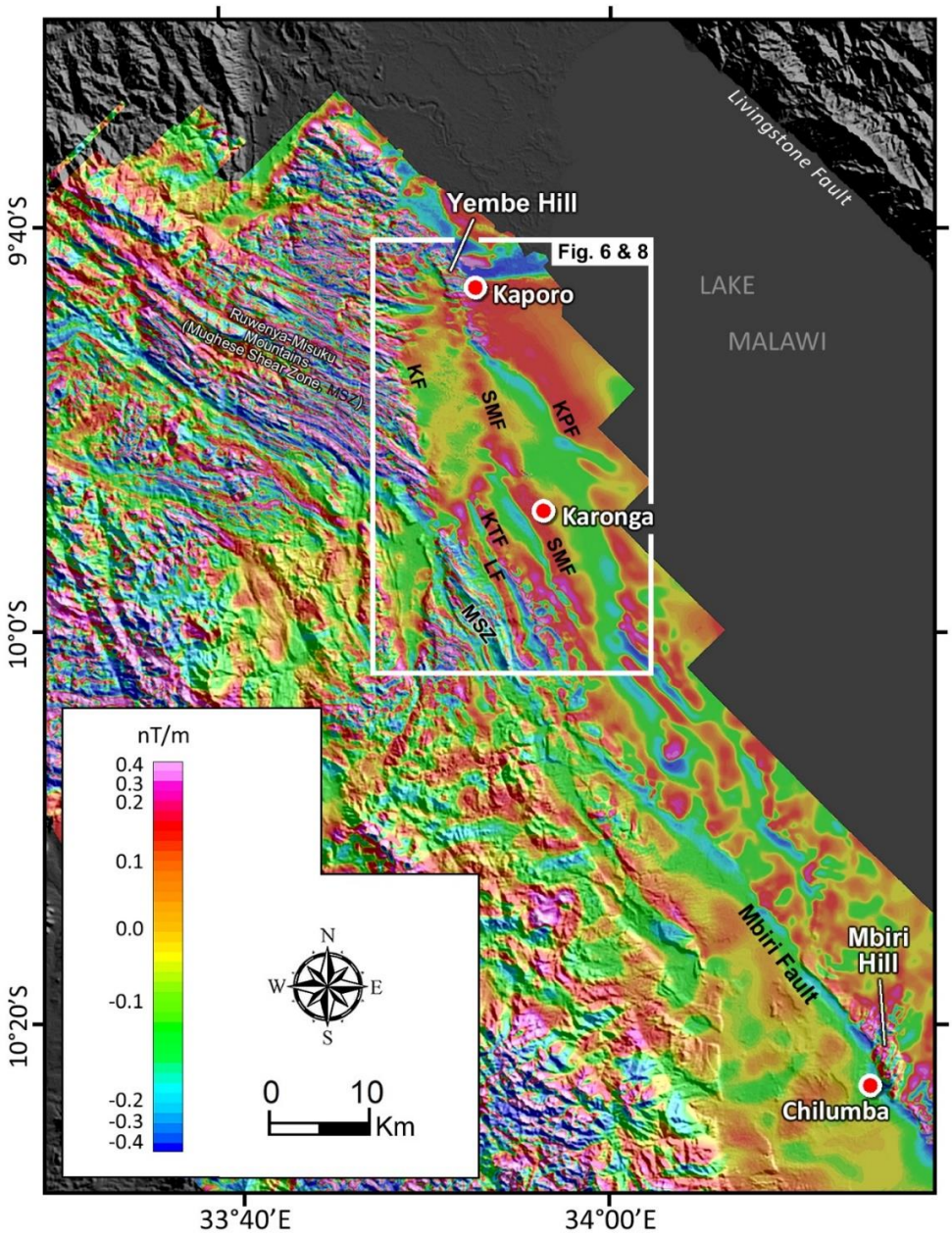


**Figure 4.** First vertical derivative of the RTP grid of the 2013 aeromagnetic map of Karonga-Chilumba area draped onto Shuttle Radar Topography Mission (SRTM) Digital Elevation Model (DEM), showing the relationship between surface morphology and structures in the basement. LF = Lupaso Fault, KPF = Kaporo Fault, KF = Karonga Fault, KTF = Katesula Fault, MSZ = Mughese Shear Zone, and SMF = St. Mary Fault.

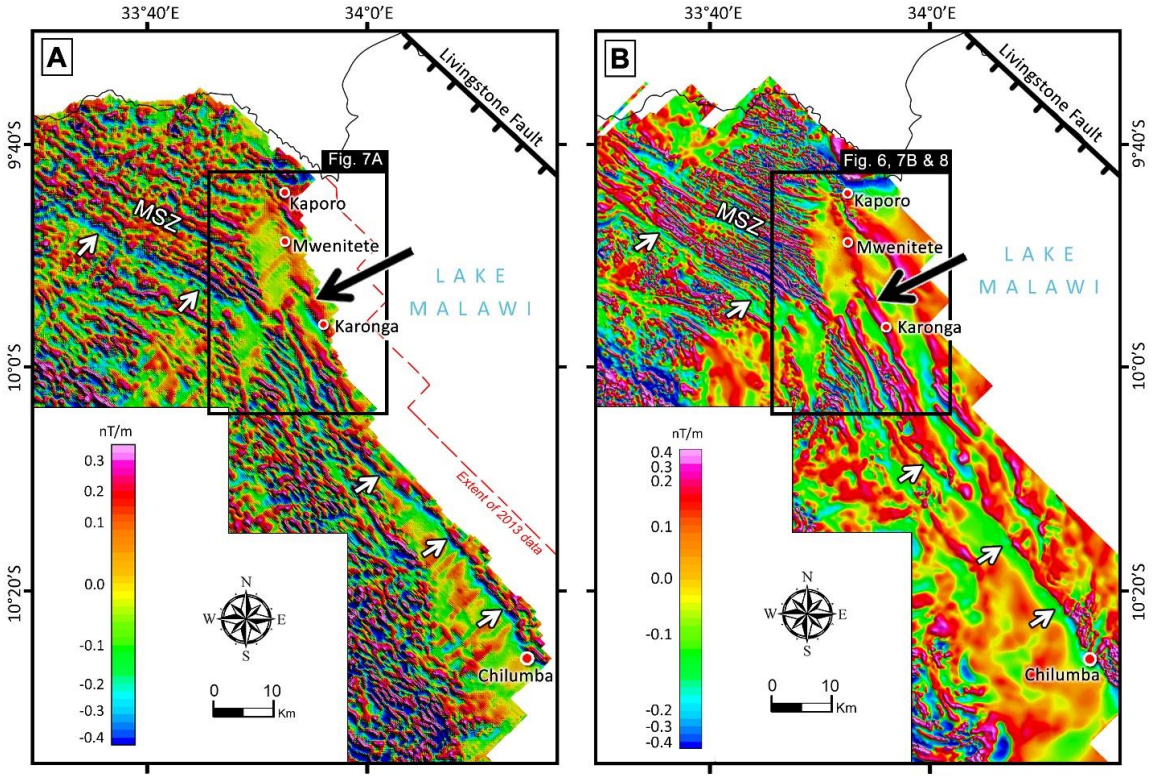


**Figure 5.** (a) First vertical derivative of the reduced to the pole (RTP) 1985 pre-earthquake aeromagnetic data of the Karonga area. (b) First vertical derivative of the RTP 2013 post-earthquake aeromagnetic data of Karonga area, upward continued to 120 m (same flight height as the 1985 map). Both aeromagnetic images show prominent magnetic lineament (black arrow) within the coastal plains of Lake Malawi. White arrows point to the magnetic expression of the southwestern boundary of the Mughese Shear Zone (MSZ).

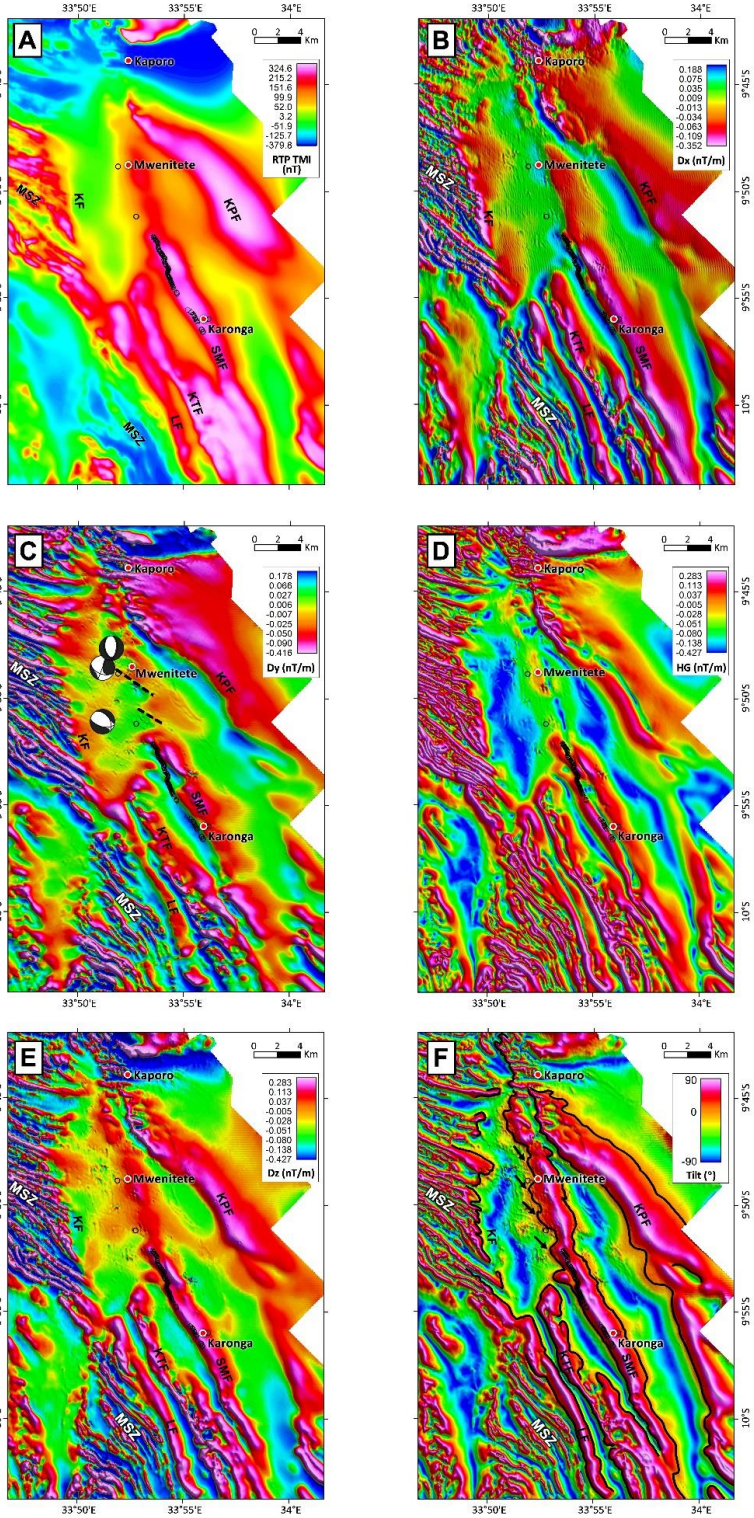
A
B
C
D
E
F
Kaporo
Mwenitete
Karonga
MSZ
KF
KPF
KTF
SMF
LF
RTP TMI (nT)
Dx (nT/m)
Dy (nT/m)
HG (nT/m)
Dz (nT/m)
Tilt (°)
0 2 4 Km
33°50'E
33°55'E
34°E
9°45'S
9°50'S
9°55'S
10°S

**Figure 6.** (a) A map of the Reduced-to-the-pole Total Magnetic Intensity (RTP-TMI) grid of Karonga area. (b) The horizontal-X derivative (Dx) of the RTP-TMI grid. (c) Horizontal-Y derivative (Dy) of the RTP-TMI grid. Fault plane solutions represent the December 2014 $M_w$ 5.1 Karonga earthquake sequence [*Oliva et al.*, 2016]. Black dotted lines show orientation of en echelon segments on the northern segment of the SMF. (d) Horizontal gradient magnitude (HG) of the RTP-TMI grid. (e) Vertical derivative (Dz) of the RTP-TMI grid. (f) Tilt derivative of the RTP-TMI grid overlaid with 0° tilt contour (solid black line). Black circles represent coseismic surface rupture locations. Black arrows point to orientation of en echelon segments on the northern segment of the SMF. LF = Lupaso Fault, KPF = Kaporo Fault, KF = Karonga Fault, KTF = Katesula Fault, MSZ = Mughese Shear Zone, and SMF = St. Mary Fault.

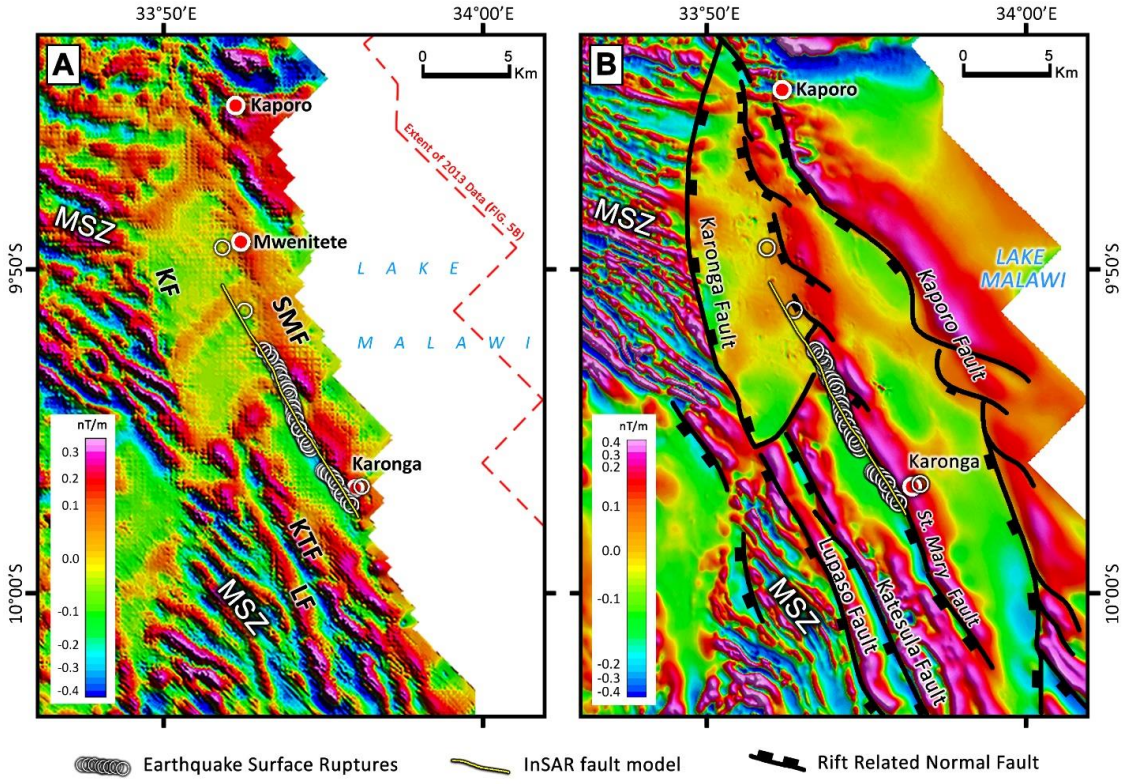


**Figure 7.** Correlation between the Interferometric Synthetic Aperture Radar (InSAR) fault model from *Biggs et al.* [2010] and *Hamiel et al.* [2012] (yellow line), mapped locations of the earthquake surface ruptures (white circles), and the prominent NNW- striking magnetic lineament representing the basement fabric in the Karonga area from (a) the 1984-1985 pre-earthquake, and (b) the 2013 post-earthquake aeromagnetic data (upward continued to 120 m). The two aeromagnetic maps are first vertical derivatives (VDR) of reduced to pole (RTP) grids of the two aeromagnetic grid vintages. LF = Lupaso Fault, KPF = Kaporo Fault, KF = Karonga Fault, KTF = Katesula Fault, MSZ = Mughese Shear Zone, and SMF = St. Mary Fault.

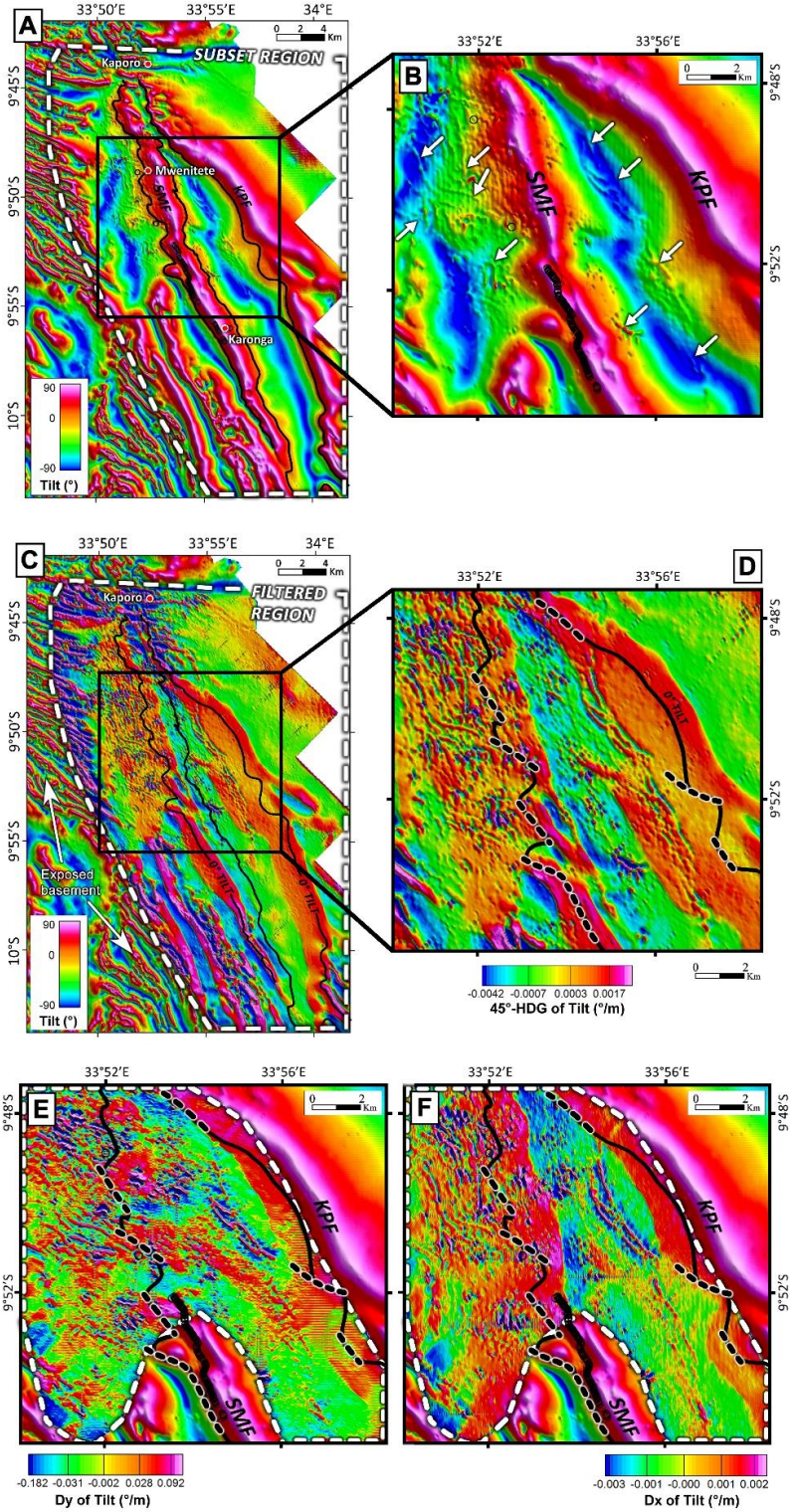
A
33°50′E
33°55′E
34°E
0 2 4 Km
SUBSET REGION
Kaporo
Mwenitete
Karonga
KPF
SMF
9°45′S
9°50′S
9°55′S
10°S
90
0
-90
Tilt (°)
B
33°52′E
33°56′E
0 2 Km
9°48′S
9°52′S
SMF
KPF
C
33°50′E
33°55′E
34°E
0 2 4 Km
FILTERED REGION
Kaporo
Exposed basement
0° TILT
0° TILT
9°45′S
9°50′S
9°55′S
10°S
90
0
-90
Tilt (°)
D
33°52′E
33°56′E
9°48′S
9°52′S
0° TILT
0 2 Km
-0.0042 -0.0007 0.0003 0.0017
45°-HDG of Tilt (°/m)
E
33°52′E
33°56′E
0 2 Km
9°48′S
9°52′S
KPF
SMF
-0.182 -0.031 -0.002 0.028 0.092
Dy of Tilt (°/m)
F
33°52′E
33°56′E
0 2 Km
9°48′S
9°52′S
KPF
SMF
-0.003 -0.001 -0.000 0.001 0.002
Dx of Tilt (°/m)

**Figure 8.** (a) Tilt derivative of the RTP 2013 aeromagnetic TMI data. SMF = St. Mary Fault, KPF = Kaporo Fault. Black circles represent the location of surface ruptures; black solid lines represent 0° contour of the tilt derivative which represents the edge of the normal faults (SMF and KPF). (b) A close-up of Figure 8a showing suppressed magnetic lineaments that are characterized by low amplitude, high frequency, short wavelength magnetic lineaments (white arrows point at some of the lineaments). (c) Tilt derivative aeromagnetic map overlaid by a subset that has been filtered using a 45° horizontal directional gradient (HDG) filter. (d) A close-up of Figure 8c. Dotted black lines show segments of the SMF and KPF that correspond to the enhanced lineaments. (e) Same window as in Figure 8d showing tilt derivative aeromagnetic map overlaid by a subset that has been filtered using a horizontal-Y filter. This subset was cut to avoid the high amplitude segments of magnetic lineaments associated with interpreted buried faults SMF and KPF. (f) Tilt derivative aeromagnetic map overlaid by a subset that has been filtered using a horizontal-X filter.

### 5.3. Geological cross-section

The edges of basement structures (zero tilt contour) are revealed by the tilt derivative of the aeromagnetic grid (Figures 6f), while the SPI map (Figure 10a and b) shows the estimate of depth to magnetic source (crystalline basement). We combine these basement models with surface topography to generate two aeromagnetic geological sections across mapped buried faults along the half-graben hinge zone (cross-sections A'-B'-C'-D' in Figures 11a-d, and E'-F' in Figures 12a-d). Here, the magnetic-high RTP-TMI anomalies over the faults are steeper to the west than to the east (Figures 11b and 12b). Along the SMF, the basement footwall cutoff is located at 508 m (in the south; Figure 11d) and 413 m (in the north; Figure 12d) depths beneath the Cenozoic lacustrine sediments. Whereas, along the KPF, the footwall cut off is at 1017 m (in the south; Figure 11d) and 748 m (in the north; Figure 12d) depths. Along the SMF and KPF, depth-to-basement generally decreases northwards. The depth-to-basement models show a distinct topographic highs

immediately east of the faults. Based on the angular relationship between the locations of the 0° tilt (at the basement level) and coseismic fault ruptures at the ground surface, we interpret a 50° dip angle for the SMF (along section A'-B'-C'-D') (Figure 11d). On the sensitivity of our dip angle estimate for the SMF, an accuracy of ±20% [*Gay,* 2009] for its 508 m footwall cut-off depth (using the SPI technique, Figure 11c) gives a range of 44°–55° dip angles. This estimate is consistent with previously published dip estimates from fault plane solutions and DInSAR analyses of coseismic events [37°–46° from *Biggs et al.*, 2010, and 41° from *Hamiel et al.*, 2012]. In the absence of information on possible coseismic ruptures along the Kaporo Fault (buried beneath the lake), we infer the same dip angle as the St. Mary Fault. Also, the cross-sections show a general eastward (basinward) decrease in basement elevation (Figures 11d and 12d) similar to previously published basement models of the North Basin [*Mortimer et al.*, 2007; *Biggs et al*., 2010], we suggest that the depth-to-basement estimates are reliable within an accuracy of ±20%.

## 6. Discussion

### 6.1. Relationship between surface rupture locations and magnetic lineaments

The mapped surface rupture locations from the 2009 Karonga earthquake align along the edge of a distinct ~37 km long, 148°-162° striking magnetic lineament in the basement that is apparent on both the pre-earthquake and post-earthquake aeromagnetic maps (black arrows on Figure 5a-b; 7a-b). We suggest that the 2009 Karonga earthquake was associated with the reactivation of a pre-existing buried basement-rooted fault that we mapped as the

SMF (Figure 4, 7a and b). The RTP-TMI anomaly over the SMF and KPF is typical of buried basement-rooted normal faults in areas where the crystalline basement is the dominant magnetic source [*Grauch and Hudson*, 2007; 2011], such that the magnetic anomaly is steepest in the direction of fault dip. The RTP-TMI anomalies over the faults are steeper to the west than to the east (Figures 11b and 12b), suggesting a west-dip for the faults and is consistent with DInSAR analyses of the earthquake [*Biggs et al.*, 2010; *Hamiel et al.*, 2012]. This dip direction indicates the faults are synthetic to the Livingstone border Fault. On the filtered aeromagnetic maps, we observe that the magnetic lineament corresponding to the SMF is segmented (Figure 6c) and that the middle section of the structure has a distinct right-stepping ~1 km-wide relay ramp across which the coseismic surface ruptures also show along-strike right-stepping pattern (Zone-2 in Figure 9).

Previous studies [e.g. *Cartwright et al*., 1995; *Fossen*, 2010] have shown that fault growth and propagation involve an initial nucleation of isolated fault segments, followed by overlapping of segments separated by relay ramps, and eventual bridging of relay ramps to allow the geometrical linkage and coalescence of the fault segments. Zone-1 of Figure 9 shows that the southern segment of the SMF (south of Karonga town) consists of coalesced right-stepping fault segments. However, north of Karonga, the fault is characterized by overlapping segments separated by a relay ramp along which the earthquake surface ruptures align (Zone-2 in Figure 9). Further north, the fault is characterized by en échelon right-stepping segments with wider relay ramps (dotted black line in Figure 6c; Zone-3 in Figure 9). The propagation of the earthquake surface ruptures

along overlapping fault segments and across the intervening relay ramp north of Karonga (Zone-2 of Figure 9) indicates that the rupture of the 2009 Karonga earthquake is associated with active deformation of the relay ramp that might ultimately lead to coalescence of fault segments along the SMF. Also, we interpret that the amplitude of the magnetic anomaly representing the SMF is significantly lower in the north (zone-3) than in the south (zone-1) (Figures 6a-e, 7 and 9) possibly due to the dominance of unlinked fault segments and shallower basement depths (and lower fault dips or lower vertical fault throws?) in the north relative to the middle and southern segments of the fault (Figures 11d and 12d). In addition, coalesced nature of fault segments in the southern part of the SMF, and the presence of relay ramps between segments in the central part of the fault and even wider relay ramps between segments in the northern portion of the fault may indicate that the 2009 earthquake event was associated with an overall northward growth of the southern segment of the fault.

We have also identified other NW, N-S and NNW-striking faults beneath the onshore area of Lake Malawi; such as KPL, KTF and LF extending from Kaporo in the north to Chilumba to the south (Figure 7b). Unpublished hypocentral relocation of the 2009 Karonga earthquake events confirm ruptures along the SMF and the KPF (personal communication, James B. Gaherty, 2017). We highlight these faults as additional buried basement-rooted faults which bound asymmetrical grabens and half-grabens. We also observe that these buried faults are synthetic to the Livingstone Fault. The basement top is located at deeper depths at the hanging wall of the KPF compared to that of the SMF, thus

suggesting that the KPF may have accommodated more displacement than other buried faults in the Karonga area (Figure 11d and 12d). This fault has a segmentation pattern similar to the SMF where NW-striking segments seem to overlap to form a NNW-SSE striking fault (Figure 9).

### 6.2. Relationship between basement structures and the Mughese Shear Zone (MSZ) fabric

The strike of the SMF changes from NNW in the south to N-S to the north (black arrow in Figure 5b points to the location of strike deflection). On the other hand, the strike of the MSZ-related magnetic lineaments change from NW in the north to NNW to the south (Figure 8a-f). This gives an apparent impression that only the southern half of the SMF aligns with the NNW-striking segment of the MSZ, while its northern half cuts across the trend of the MSZ. However, detailed delineation of the orientation of segments of the SMF reveals that its northern half is made-up of several short en-echelon NW-NNW-striking fault segments (dotted black lines in Figures 8d-f). We observe that the strike of these short en echelon segments is consistent with the nodal planes on the fault plane solution of one of the seismic events (southernmost fault plane solution in Figure 6c) associated with the 2014 $M_w$ 5.1 Karonga earthquake sequence [*Oliva et al.*, 2016]. Its southern half, however, is made up of longer en-echelon NNW-striking segments that propagate along the fabric of the MSZ (Figures 6c-e and 7b). The southern segments of the SMF show coalescence while its northern segments might eventually coalesce to form a more penetrative N-

trending fault. The coalescence of fault segments that originally reactivated the MSZ basement fabric results in an overall fault geometry that appears to cut obliquely across the MSZ basement fabric. Based on the enhanced trend of the MSZ-related lineaments underlying the sedimentary cover (Figures 8d-f), and interpreted the map-view geometry of the buried KPF, KTF, LF and SMF faults (e.g. shown by the geometry of the 0° tilt contour in Figures 8d-f and interpretation on Figure 9), we interpret an alignment of segments of the faults with the southeast continuation of the MSZ basement fabric (Figure 13). The trend of the MSZ switches from NW-strike in the northwest to a NNW-strike in the Karonga area and back to a NW-strike in the southeast between Karonga and Chilumba towns (white lines in Figure 13). This indicates a subtle right-stepping bend of the MSZ. The trend of the magnetic anomalies manifesting the southwestern boundary of the shear zone also suggests this geometry (white arrows in Figure 5a and b). Therefore, the alignment of segments of the SMF, KPF, KTF, LF and MF with the MSZ fabric suggest that these faults exploited the basement fabric. Farther south of Karonga town, the reactivation of the southeastern segment of the MSZ is shown by the alignment of magnetic lineaments with the MF which crops out at Chilumba town and bounds the Mbiri Hill in the west (Figure 4 and 13). Although the presence of Late Carboniferous - Early Jurassic sedimentary rocks along the scarp of the KF suggests that the fault is related to Karoo rifting (Figure 3a), we suggest that a better understanding of the syntectonic stress-field may provide insight into the mechanics of propagation of the fault across the fabric of the MSZ.

Studies [e.g. *Bell*, 1996; *Zang and Stephansson*, 2010; *Morley*, 2010] have shown that geomechanical property contrasts can cause local reorientation of stresses (herein referred to as stress rotations), such that where the discontinuity is relatively weak the maximum principal stress and maximum horizontal stress ($S_{Hmax}$) directions will deflect sub-parallel to the discontinuity. Where the material is relatively strong (stiff), the maximum principal stress and $S_{Hmax}$ will deflect sub-perpendicular to the discontinuity. *Morley* [2010] demonstrated that basement domains with well-defined metamorphic foliation and mylonitic fabric are zones where stress rotations can occur. In northern Malawi, although it is suggested that the direction of regional extension has changed over time [e.g. *Ring*, 1994; *Mortimer* et al., 2007], the E-W present-day extension direction [*Saria et al.*, 2014] is sub-orthogonal to the overall trend of the SMF (White arrows in Figure 13). Therefore, we suggest that the obliquity of the SMF with respect to MSZ basement fabric is effectively controlled by local stress rotations from the regional E-W extension direction (minimum principal stress) into a plane that is sub-orthogonal to the trend of the MSZ fabric. Thus, the stress rotation is locally resolved as normal displacement reactivating obliquely-oriented basement fabric.

Previously published DInSAR models of the 2009 Karonga earthquake [*Biggs et al.*, 2010; *Hamiel et al*., 2012] and our modeling of depth-to-magnetic-source (crystalline basement) from high resolution aeromagnetic data (Figure 11d) reveal a 37°-50°SW dip angle for the ruptured faults (SMF and other faults along the half-graben hinge zone). Although we observe that the faults follow basement fabric along-strike, the estimated dip

angle of the faults are shallower than the relatively steeper sub-vertical dip angles (60°-85°) of the MSZ basement fabric [Figures 3b and c;

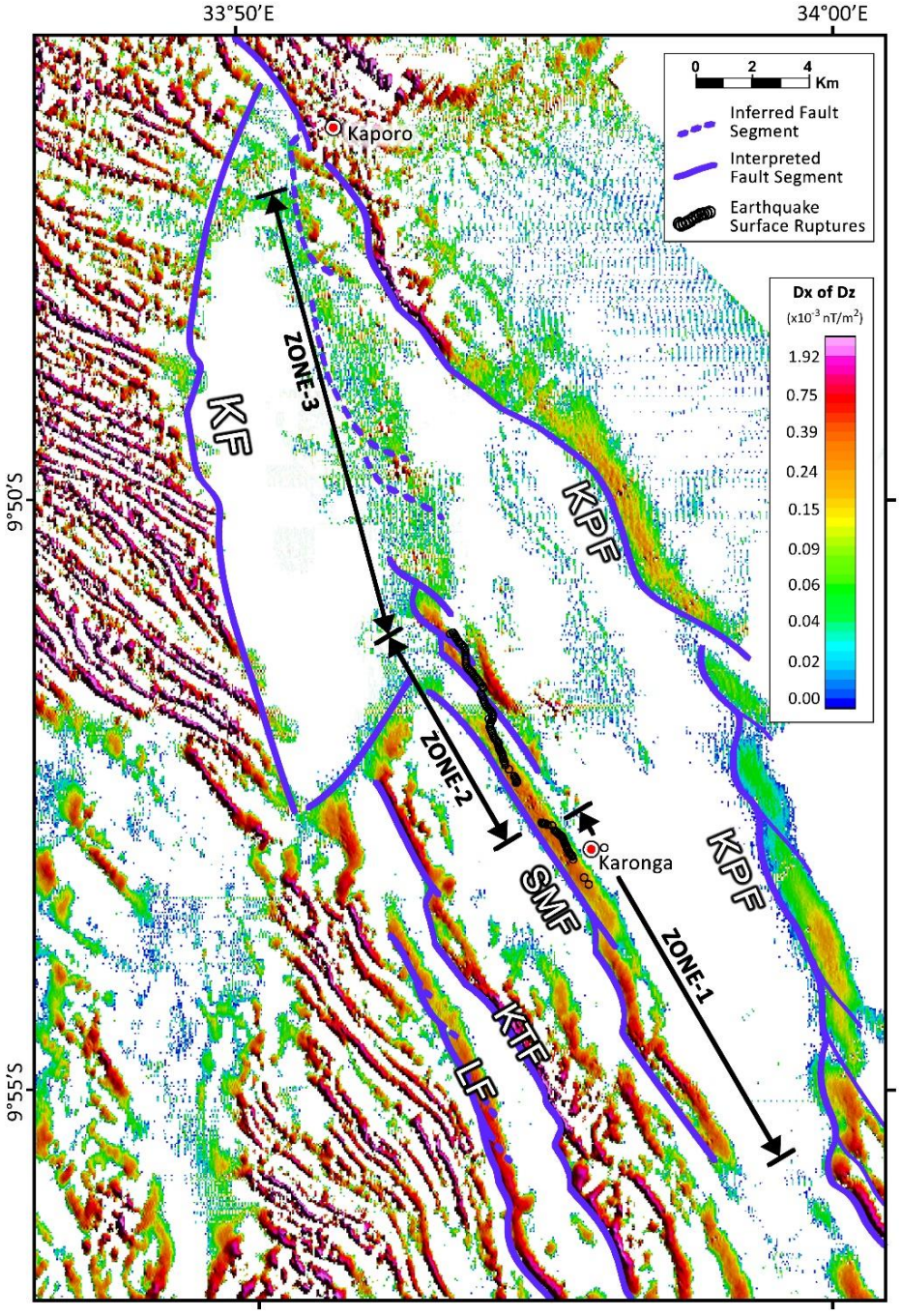

**Figure 9.** Horizontal-X derivative of the vertical derivative of the 2013 aeromagnetic grid covering the Karonga area showing enhanced along-strike geometry of the ruptured St. Mary Fault (SMF) and other buried faults in the area including Kaporo Fault (KPF), Katesula Fault (KTF), and Lupaso Fault (LF). Zone-1: Fault interpretation shows that the southern segment of SMF is dominated by coalesced fault segments. Zone-2: North of Karonga town, the SMF is characterized by overlapping segments separated by ~1 km-wide relay ramp. Also shown are the earthquake surface ruptures bridging this relay ramp (black circles). Zone-3: Farther north, the SMF is characterized by en-echelon segments and wider relay gaps (inferred from Figure 6c and f).

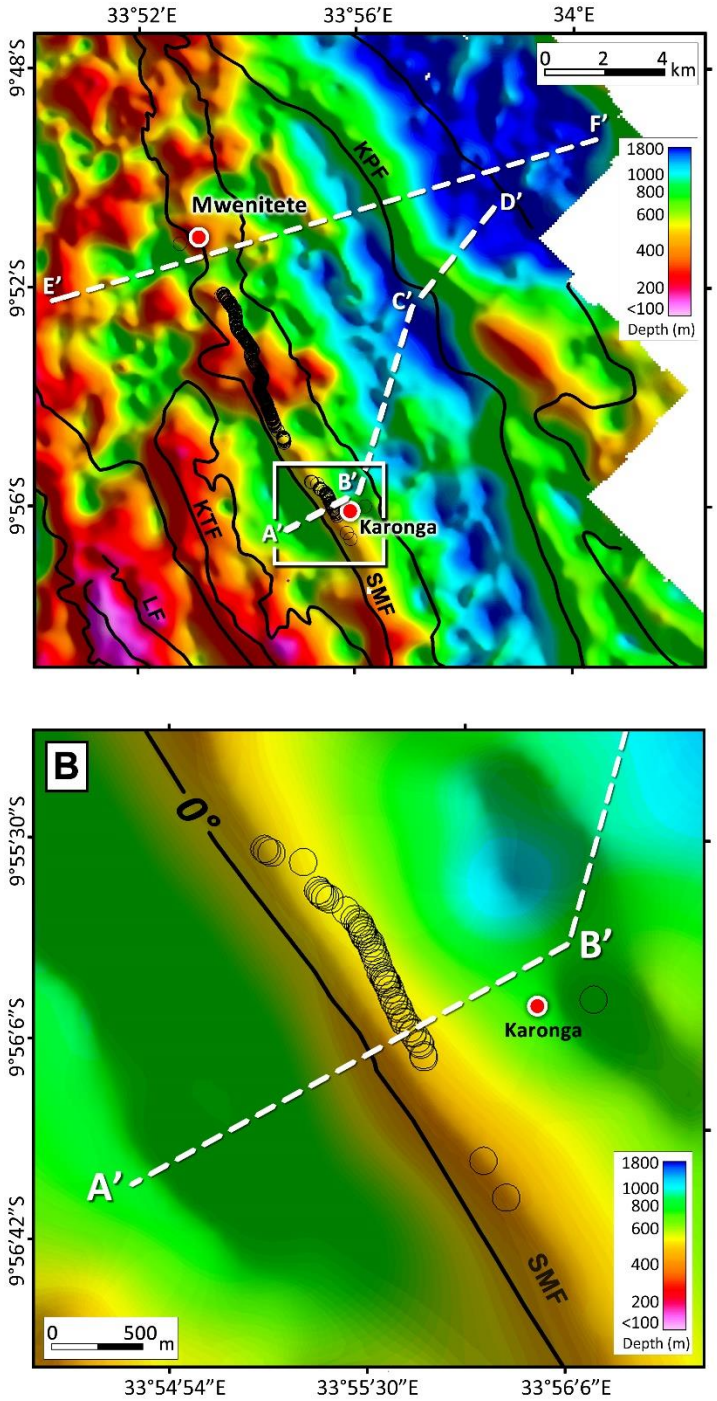


**Figure 10.** (a) Depth to basement map of Mwenitete – Karonga area calculated using the Source Parameter Imaging (SPI) technique, overlain with surface rupture locations (black

circles). Bold contours represent the zero-degree tilt contour (representing the edge of the basement faults). White dotted lines represent transects for cross-sections A'-B'-C'-D' and E'-F' in Figures 11 and 12. (b) Depth-to-basement map of Karonga area (area in white box in Figure 10a) showing the location of the zero-degree tilt contour relative to the location of surface ruptures along-strike of the SMF.

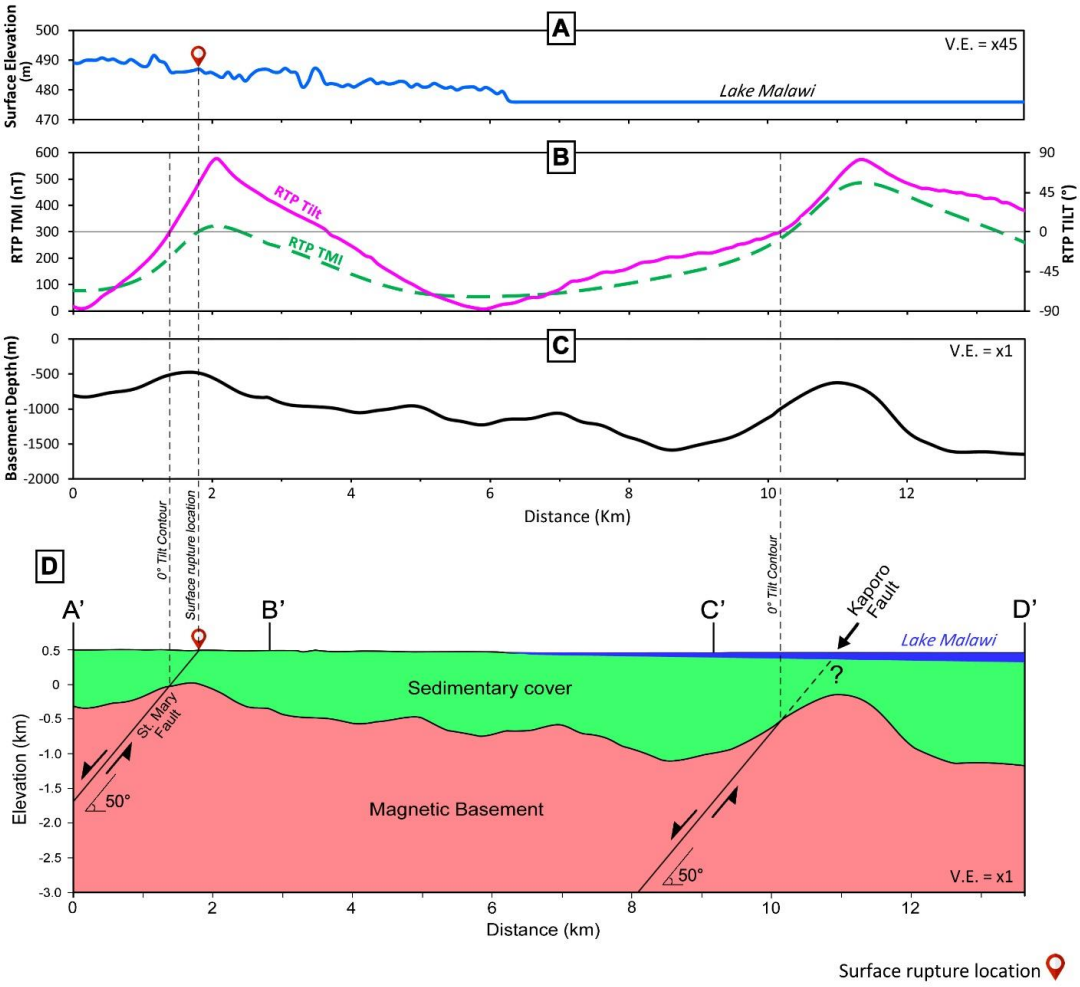


**Figure 11.** (a) Surface elevation, (b) Reduced-to-the-pole total magnetic intensity (RTP-TMI) and tilt derivative (RTP Tilt), and (c) Depth to magnetic basement, along cross-section A'-B'-C'-D' (see Figure 10a for location). (d) Aeromagnetic geological cross-section along section A'-B'-C'-D'. We estimate a 50° dip angle for the St. Mary Fault

(SMF) based on the angular relationship between the locations of the 0° tilt (at basement surface) and the surface fault ruptures. Since possible coseismic surface ruptures along the Kaporo Fault (KPF) are buried beneath the lake, we infer the same dip angle as the St. Mary Fault.

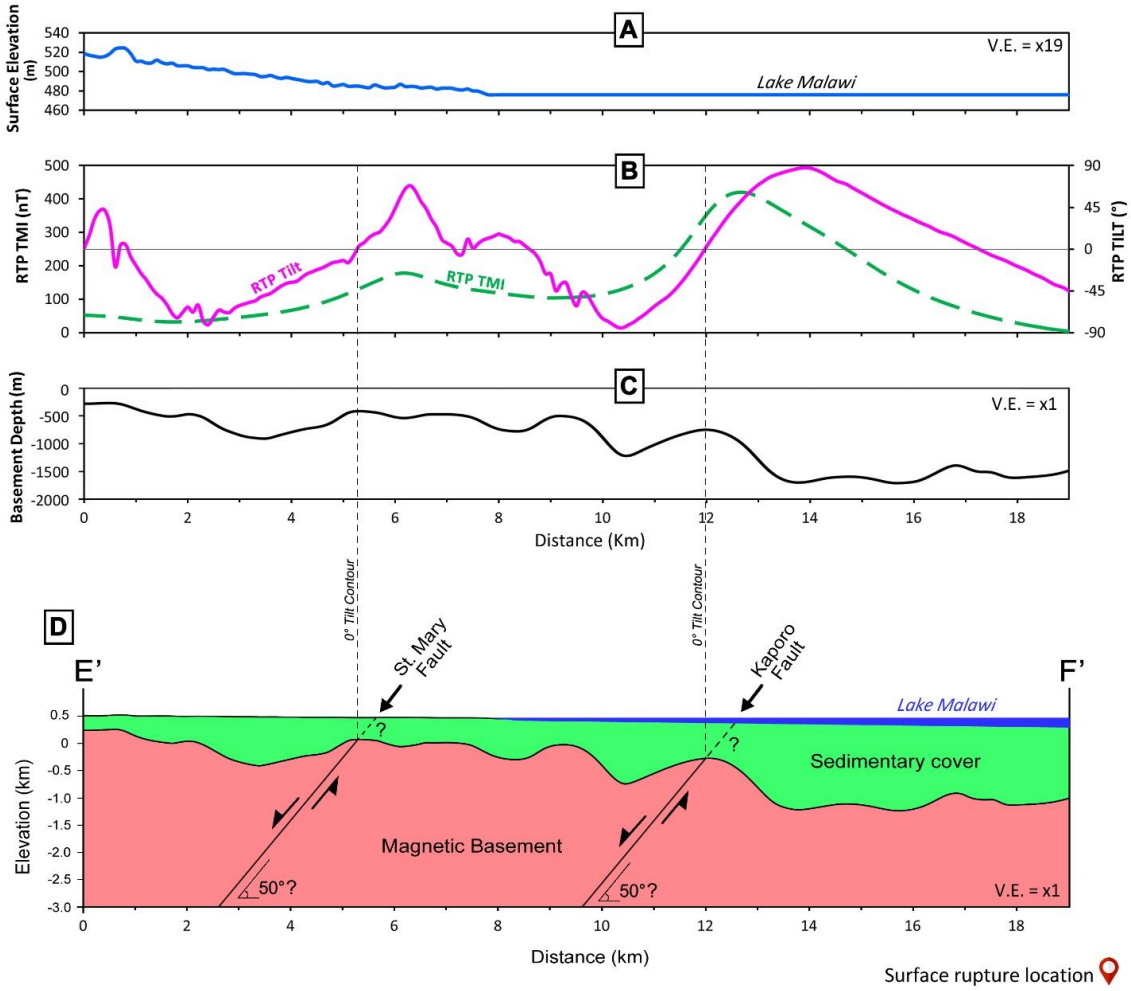


**Figure 12.** (a) Surface elevation, (b) Reduced-to-the-pole total magnetic intensity (RTP-TMI) and tilt derivative (RTP Tilt), and (c) Depth to magnetic basement, along cross-section E'-F' (see Figure 10a for location). (d) Aeromagnetic geological cross-section along section E'-F'. We infer a 50° dip angle for the St. Mary Fault (SMF) and Kaporo Fault (KPF) based on results in Figure 11d.

*Ring*, 1993]. Several studies have reported the development of younger faults parallel to the strike of basement fabric, which cut this fabric obliquely down-dip [e.g. *Morley*, 1995; *Ring et al*., 2005; *Morley*, 2010]. *Morley* [2010] observed low-angle (20°-30°) normal faults reactivating along basement foliation within the Rukwa Rift, and attributed the fault development to stress rotations; such that the dip angle defining the least cohesive shear strength for the propagation of the normal faults was 30° away from the rotated maximum principal stress (dip of the foliation). We suggest that the reactivation of the MSZ basement fabric into normal faults that follow the fabric along strike but develop into a lower-angle fault down-dip can be explained by the stress-rotation model of *Morley* [2010]. According to this model, the normal fault that subsequently develops from reactivation by stress rotations will appear to obliquely cut foliation down dip with at angular difference of ~30°. Based on this model, the 60°-85° dips of the MSZ basement fabric in the Karonga area should reactivate into normal faults with ~30°-55° dip angles, thus explaining the relatively shallow 37°-50° dip angle of the buried basement faults in Karonga area as compared to the steeper dip angles of the MSZ basement fabric.

### 6.3. Half-graben hinge zone deformation

Figures 14a and b shows the spatial distribution of the earthquake epicenters associated with the 2009 Karonga seismic event. This distribution shows that the majority of the earthquakes cluster in the region bounded by the KPF in the east, the KF to the west, and the area just west of the LF where the MSZ outcrops (area bounded by the dashed white

ellipse in Figure 14a). We suggest that although most of the $M_w \geq 4.9$ events as well as significant ground displacement during the 2009 earthquake swarm were localized along the SMF, the other identified buried basement faults underlying the Karonga area (KPF, KTF, LF and MF) might have also accommodated some of the deformation. In addition, the spatial distribution of epicenters with respect to the entire North Basin of the Malawi Rift suggests that active deformation associated with the 2009 seismic events is localized within the half-graben hinge zone (Figure 14b) and not distributed across the entire hanging-wall as suggested by *Biggs et al*. [2010]. The location of seismic events west of the east-dipping KF (Figure 14a and b) may suggest that the planes of the SMF and KPF (west-dipping) undercut the KF down-dip, thereby highlighting the need to better understand the subsurface interaction of the faults along the half-graben hinge zone.

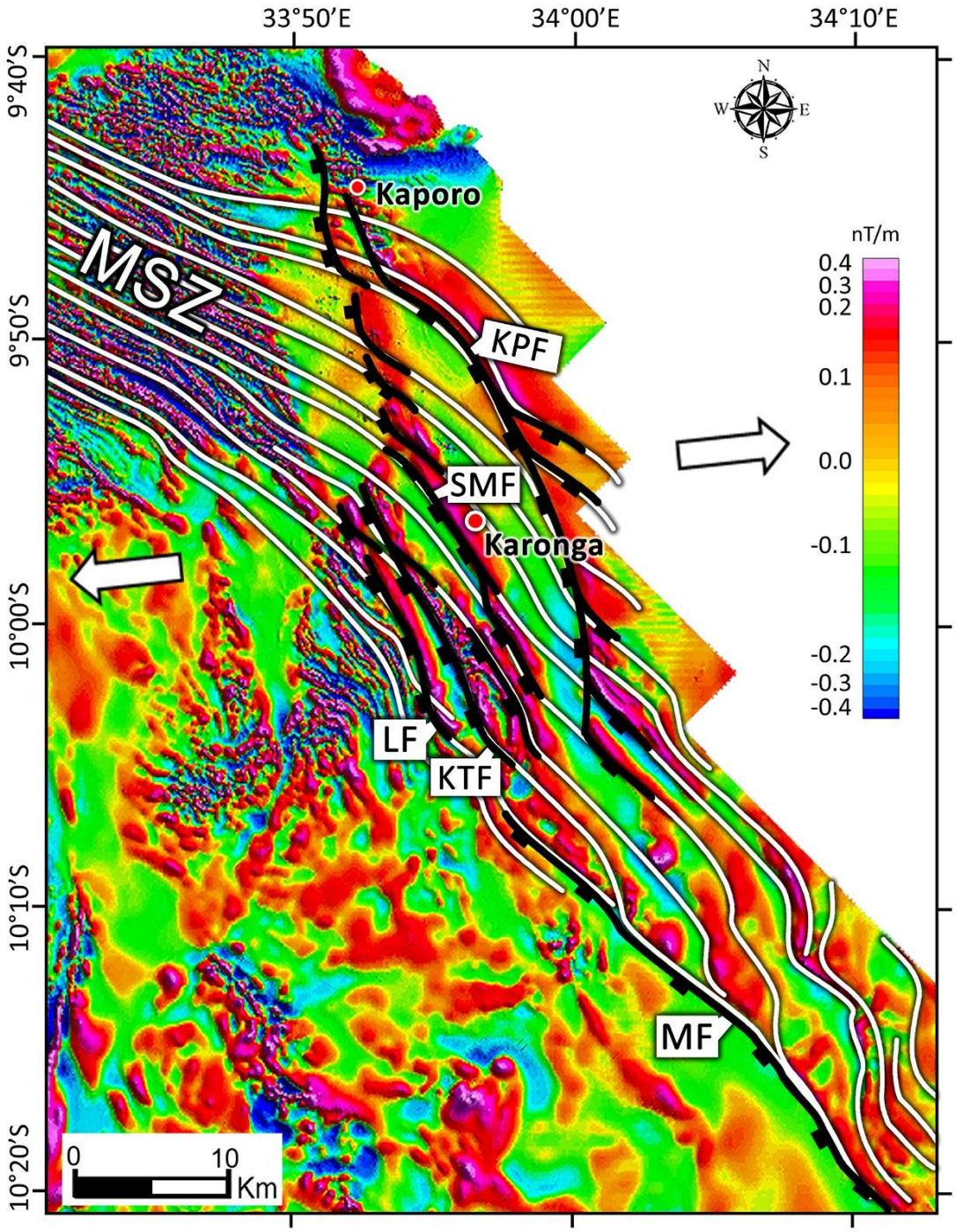
33°50'E
34°00'E
34°10'E
9°40'S
9°50'S
10°00'S
10°10'S
10°20'S
N
W
E
S
Kaporo
MSZ
KPF
SMF
Karonga
LF
KTF
MF
nT/m
0.4
0.3
0.2
0.1
0.0
-0.1
-0.2
-0.3
-0.4
0
10
Km

**Figure 13.** First vertical derivative of the 2013 aeromagnetic data of the Karonga area showing the superposition of blind faults buried beneath the sedimentary cover (black solid lines, labelled faults) on the interpreted overall trend of the Mughese Shear Zone (MSZ) fabric (white solid lines). White arrows indicate present-day extension direction. KPF = Kaporo Fault, KTF = Katesula Fault, LF = Lupaso Fault, SMF = St. Mary Fault and MF = Mbiri Fault.

Models proposed for the development of half-graben rift basins generally assume that the hinge zones of half-grabens are mainly flexural margins with brittle deformations that develop passively in response to progressive displacement along the border fault [e.g. *Rosendahl et al*., 1986; *Groshong*, 1989; *Schlische*, 1991; *Seyitoglu et al*., 2002]. We alternatively suggest that the localization of upper crustal strain and seismicity on the half-graben hinge zone of the North Basin in the weakly extended, magma-poor Malawi Rift is not entirely driven by a passive crustal flexure of the border fault hanging-wall, but is being facilitated by the presence of favorably-oriented basement fabric. We further suggest that the influence of the MSZ on the large-scale structural architecture of the North Basin may be most evident in the relatively lower dip angles of the hinge zone faults (<50°) compared to that of the intrabasin faults and border fault (55° - 60°; *Wheeler and Karson*, 1989; *Mortimer et al.*, 2007) (Figure 14b).

### 6.4. Implications for earthquake hazards

Our study shows that the surface ruptures occurred mostly along the central part of the SMF with a total length of 16.4 km, covering half the length of the 37 km-long fault

(Figures 7 and 9). We point to the high potential for frequent brittle failure along the unruptured, soft-linked, en echelon northern segments of the SMF between Karonga and Kaporo towns in the future (Zone-3 in Figure 9). The presence of longer fault segments on the southern part of the SMF (Zone-1 in Fig. 9) relative to its northern segments (Zone-3 in Fig. 9) suggest that the southern segment of the SMF is capable of bigger earthquakes if it were to rupture. The fact that the southern segment has not ruptured recently may indicate that it is a seismic gap with potential of future rupture. Following standard scaling magnitude-length relationship [e.g., *Wells and Coppersmith*, 1994; *Field et al*., 2003], an earthquake of $M_w 6.4 \pm 0.34$ (mean magnitude) could occur if this entire 'seismic gap' were to rupture in a single event. Overall, due to the presence of en echelon segmentation of the SMF in the north than in the south, we predict a relatively higher probability for frequent seismic activities in the northern part of Karonga area than in the south. This prediction is supported by the $M_w$ 5.1 2014 Karonga earthquake sequence reported by *Oliva et al.* [2016]. The epicenters of this earthquake event were located ~3 km west and 5 km SW of Mwenitete town (yellow stars in Figure 14a); however, hypocentral depths of 5-10 km suggest that the rupture possibly occurred down-dip of the SMF and/or KPF. We also raise the possibility that the extents of the KPF, KTF, LF and MF present favorable sites for future brittle rupture leading to seismic activities along the half-graben hinge zone. We present an updated fault map of the North Basin, showing the possible seismogenic faults along the half-graben hinge zone (Figure 15).

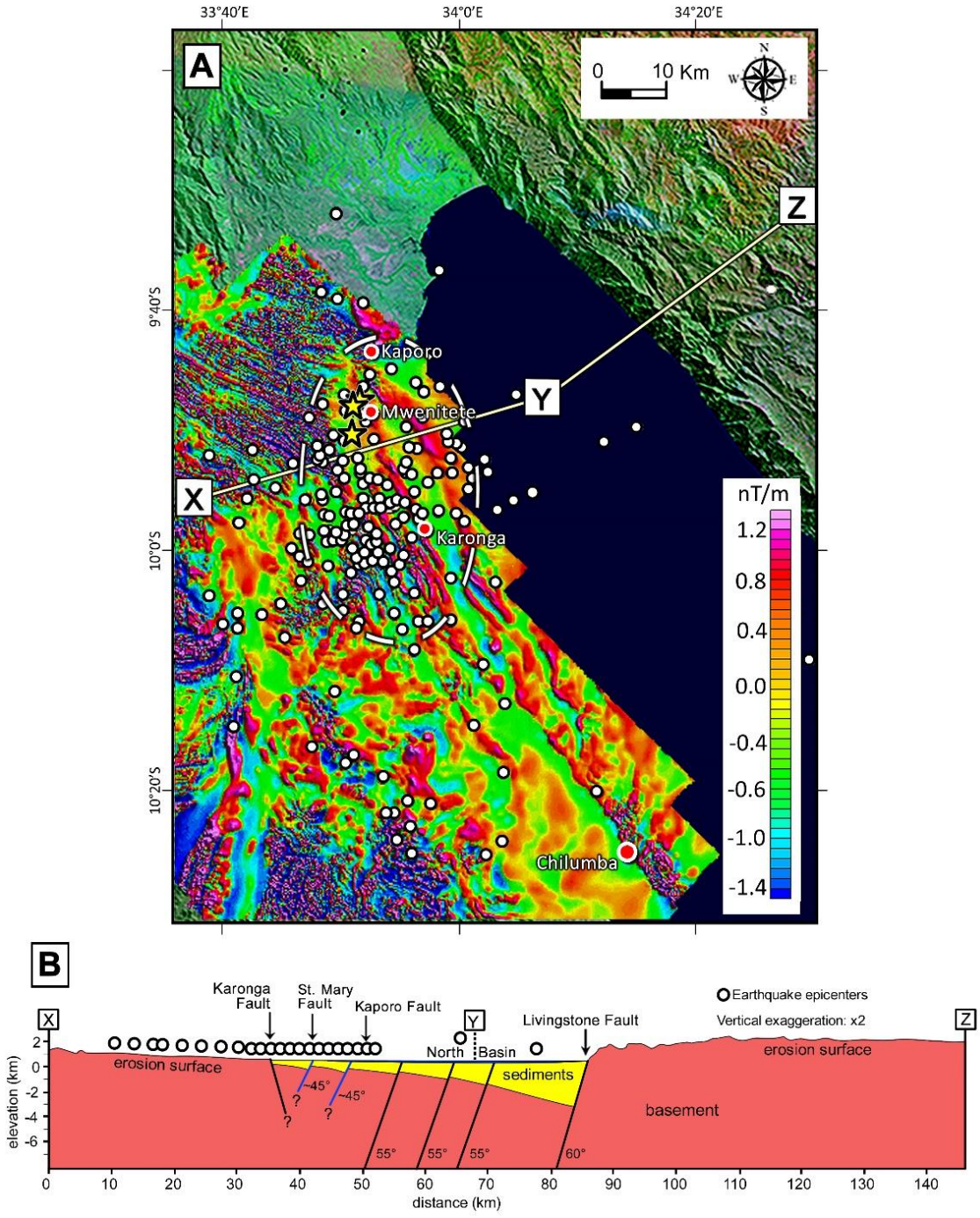
A
33°40′E
34°0′E
34°20′E
9°40′S
10°0′S
10°20′S
0
10 Km
N
W
E
S
X
Y
Z
Kaporo
Mwenitete
Karonga
Chilumba
nT/m
1.2
0.8
0.4
0.0
-0.4
-0.6
-1.0
-1.4
B
Karonga Fault
St. Mary Fault
Kaporo Fault
Livingstone Fault
Earthquake epicenters
Vertical exaggeration: x2
North Basin
erosion surface
sediments
basement
~45°
55°
60°
elevation (km)
distance (km)

**Figure 14.** (a) First vertical derivative of the Reduced to Pole (RTP) aeromagnetic map of Karonga area overlaid on 742 (Red-Green-Blue) Landsat Thematic Mapper (TM) image (draped onto Digital Elevation Model) showing the location of the epicenters of earthquakes associated with the 2009 Karonga earthquake swarm (white dots). The ellipse defined by dashed white line defines the area with the greatest clustering of earthquake epicenters. Yellow stars (around Mwenitete) represent the epicenters of the $M_w$ 5.1 2014 Karonga earthquake sequence reported by *Oliva et al*. [2016] (also shown in Figure 6c). (b) Cross-section along baseline X-Y-Z shown in Figure 10a across the North Basin [modified after *Biggs et al*; 2010], showing major faults and the projection of earthquake epicenters (white circles) to the profile line. We modify this previously published cross-section based on basement depths in Figure 12d, fault dips from this study, *Mortimer et al.* [2007] and *Wheeler and Karson* [1989]. The projected earthquake epicenters (associated with the 2009 Karonga earthquake swarm) cluster on the hinge zone of the North Basin half-graben.

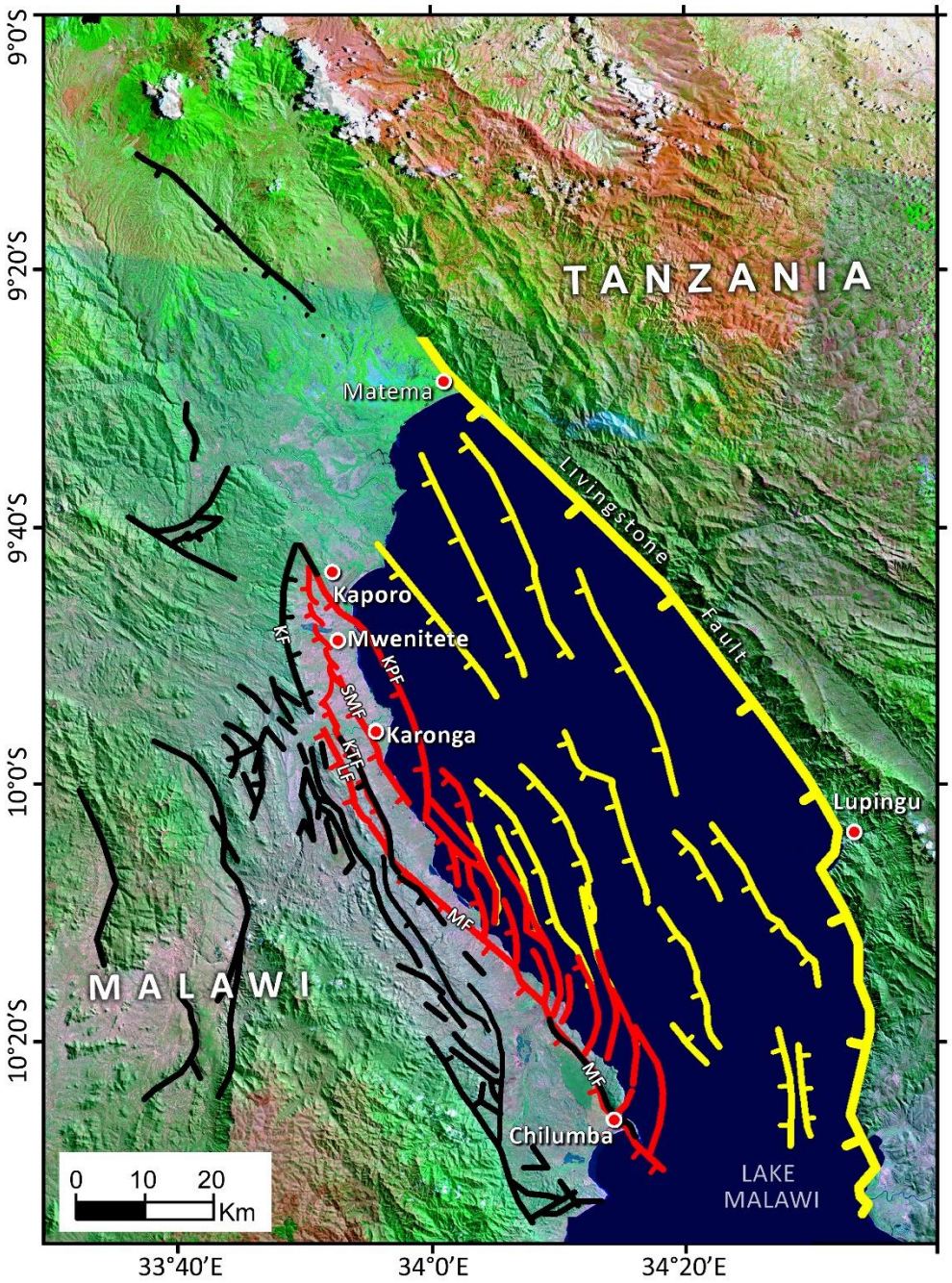


**Figure 15.** 742 (Red-Green-Blue) Landsat Thematic Mapper (TM) image draped onto Shuttle Radar Topography Mission (SRTM) Digital Elevation Model (DEM) of the North Basin. Red lines represent newly identified faults (from aeromagnetic data) along the hinge zone of the basin; yellow lines represent faults interpreted from seismic data [from

*Mortimer et al*., 2007]; black lines represent faults observable on SRTM [reported in previously published maps e.g. Figure 3a] and aeromagnetic maps. KF = Karonga Fault, KPF = Kaporo Fault, KTF = Katesula Fault, LF = Lupaso Fault, MF = Mbiri Fault, SMF = St. Mary Fault.

## 7. Conclusions

We documented for the first time, the presence of seismogenic buried basement faults along the half-graben hinge zone that could potentially be sites of future brittle rupture that will trigger earthquakes. From the analysis of pre-earthquake and post-earthquake aeromagnetic data and field observation, we delineated the along-strike geometry and dip angle of the SMF that ruptured during the 2009 Karonga earthquake. We also identified other potential seismogenic buried faults in the area and showed that the recent seismicity along the ruptured SMF is associated with overall northward development of the SMF, and geometrical linkage and coalescing of initially overlapped segments. In addition, we suggest the reactivation of sub-vertical basement fabric along the North Basin half-graben hinge zone by stress rotation. Fault geometries, basement fabric analyses, and spatial distribution of recent seismicity in the magma-poor, weakly-extended northern Malawi Rift suggest that focusing of upper crustal deformation leading to moderate-magnitude seismicity along the half-graben hinge zone may not be entirely driven by crustal flexure, but may also be facilitated and modulated by the MSZ basement fabric. Careful analysis of aeromagnetic data can play an important role in delineating causative faults associated with damaging seismic events and can therefore help earthquake mitigation efforts.

**Acknowledgements**

This work was partially supported by the National Science Foundation (NSF) grant no. II – 1358150 and NSF-EAR 1255233. We thank the Geological Survey Department of Malawi for allowing us to purchase the 2013 aeromagnetic data used in this study. The old (1984/85) aeromagnetic data used in this study can be obtained from the Council for Geosciences, South Africa. We thank two anonymous reviewers for detailed and constructive reviews.

**References**

Arkani-Hamed, J. (1988), Differential reduction-to-the-pole of regional magnetic anomalies, *Geophysics*, *53*, 1592–1600.

Baranov, V. (1957), A new method for interpretation of aeromagnetic maps: Pseudo-gravimetric anomalies, *Geophysics*, *22*, 359-383.

Beacom, L. E., R. E. Holdsworth, K. J. W. McCaffrey, and T. B. Anderson (2001), A quantitative study of the influence of pre-existing compositional and fabric heterogeneities upon fracture-zone development during basement reactivation, *Geol. Soc., London, Spec. Pub.*, *186*(1), 195-211.

Bell, J. S. (1996), In situ stresses in sedimentary rocks (part 2): applications of stress measurements. *Geosci. Can.*, *23*(3), 135–153.

Biggs, J., E. Nissen, T. Craig, J. Jackson, and D. P. Robinson (2010), Breaking up the hanging wall of a rift-border fault: the 2009 Karonga earthquakes, Malawi, *Geoph. Res. Lett., 37*, L11305.

Bott, M. H. (1997), Modeling the formation of a half graben using realistic upper crustal rheology, *J. Geoph. Res.: Solid Earth*, 102(B11), 24605-24617.

Calais, E., N. d'Oreye, J. Albaric, A. Deschamps, D. Delvaux, J. Déverchere, C. Ebinger, R. W. Ferdinand, F. Kervyn, A. S. Macheyeki, and A. Oyen (2008), Strain accommodation by slow slip and dyking in a youthful continental rift, East Africa, *Nature, 456*(7223), 783-787.

Carter, G. S., and J. D. Bennett (1973), The geology and mineral resources of Malawi (2nd revised edition), *Geol. Surv. of Malawi Bull., 6*, 62.

Cartwright, J. A., B. D. Trudgill, and C. S. Mansfield (1995), Fault growth by segment linkage: an explanation for scatter in maximum displacement and trace length data from the Canyonlands Grabens of SE Utah, *J. Struct. Geol*., *17*(9), 1319-1326.

Castaing, C. (1991), Post-Pan-African tectonic evolution of South Malawi in relation to the Karroo and recent East African rift systems, *Tectonophysics*, *191*(1-2), 55-73.

Chorowicz, J. (2005), The East African rift system, *J. African Earth Sci., 43*, 379–410.

Corti, G., J. van Wijk, S. Cloetingh, and C. K. Morley (2007), Tectonic inheritance and continental rift architecture: Numerical and analogue models of the East African Rift system, *Tectonics*, *26*(6).

Craig, T. J., J. A. Jackson, K. Priestley, and D. McKenzie (2011), Earthquake distribution patterns in Africa: their relationship to variations in lithospheric and geological structure, and the rheological implications, *Geoph. J. Int.*, *185*, 403-434.

Daly, M. C., J. Chorowicz, and J. D. Fairhead (1989), Rift basin evolution in Africa: the influence of reactivated steep basement shear zones, *Geol. Soc., London, Special Publications*, *44*(1), 309-334.

Ebinger, C. J., and M. Casey (2001), Continental breakup in magmatic provinces: An Ethiopian example, *Geology, 29*(6), 527–530.

Ebinger, C. J., A. L. Deino, R. Drake, and A. L. Tesha (1989), Chronology of volcanism and rift basin propagation: Rungwe Volcanic Province, East Africa, *J. Geophys. Res., 94*, 15785–15803.

Fagereng, Å. (2013), Fault segmentation, deep rift earthquakes and crustal rheology: Insights from the 2009 Karonga sequence and seismicity in the Rukwa–Malawi rift zone, *Tectonophysics, 601*, 216-225.

Field, E. H., T. H. Jordan, and C. A. Cornell (2003), OpenSHA: A developing community-modeling environment for seismic hazard analysis, *Seis. Res. Lett.*, *74*(4), 406-419.

Fossen, H. (2010), Structural Geology, *Cambridge Univ. Press, New York*, 463.

Fritz, H., M. Abdelsalam, K. A. Ali, B. Bingen, A. S. Collins, A. R. Fowler, W. Ghebreab, C. A. Hauzenberger, P. R. Johnson, T. M. Kusky, and P. Macey (2013), Orogen styles in the East African Orogen: a review of the Neoproterozoic to Cambrian tectonic evolution, *Jour. Afr. Earth Sciences, 86*, 65-106.

Gay Jr., S. P. (2009), Reactivation tectonics: The evidence and the consequences, American Stereo Map Co., Salt Lake City, Utah.

Goldsworthy, M., and J. Jackson (2001), Migration of activity within normal fault systems: Examples from the Quaternary of mainland Greece, *J. Struct. Geol.*, *23*, 489–506.

Grauch, V. J. S., and M. R. Hudson (2007), Guides to understanding the aeromagnetic expression of faults in sedimentary basins: Lessons learned from the central Rio Grande rift, New Mexico, *Geosphere*, *3*(6), 596-623.

Grauch, V. J. S., and M. R. Hudson (2011), Aeromagnetic anomalies over faulted strata, *The Leading Edge*, *30*(11), 1242-1252.

Groshong, R. H. (1989), Half-graben structures: Balanced models of extensional fault-bend folds, *Geol. Soc. of Amer. Bull.*, *101*(1), 96-105.

Hamiel, Y., G. Baer, L. Kalindekafe, K. Dombola, and P. Chindandali (2012), Seismic and aseismic slip evolution and deformation associated with the 2009–2010 northern Malawi earthquake swarm, East African Rift, *Geophys. J. Int.*, *191*, 898–908.

Hussein, H. M., I. Marzouk, A. R. Moustafa, and N. Hurukawa (2006), Preliminary seismicity and focal mechanisms in the southern Gulf of Suez: August 1994 through December 1997, *J. Afr. Earth Sci.*, *45*(1), 48-60.

Jacobs, L. L., D. A. Winkler, Z. M. Kaufulu, and W. R. Downs (1990), The dinosaur beds of northern Malawi, Africa, *Nat. Geo. Res.*, *6*(2), 196-204.

Katumwehe, A. B., M. G. Abdelsalam, and E. A. Atekwana (2015), The role of pre-existing Precambrian structures in rift evolution: The Albertine and Rhino grabens, Uganda, *Tectonophysics*, 646, 117-129.

Kearey, P., K. A. Klepeis, and F. J. Vine (2009), Global Tectonics, *John Wiley & Sons*.

Kinabo, B. D., E. A. Atekwana, J. P. Hogan, M. P. Modisi, D. D. Wheaton, and A. B. Kampunzu (2007), Early structural development of the Okavango rift zone, NW Botswana, *J. of Afric. Earth Sci., 48*, 125-136.

Kinabo, B. D., J. P. Hogan, E. A. Atekwana, M. G. Abdelsalam, and M. P. Modisi (2008), Fault growth and propagation during incipient continental rifting: insights from a combined aeromagnetic and Shuttle Topography Mission digital elevation model investigation of the Okavango Rift Zone, northwest Botswana, *Tectonics, 27*, 1-16.

Laó-Dávila, D. A., H. S. Al-Salmi, M. G. Abdelsalam, and E. A. Atekwana (2015), Hierarchical segmentation of the Malawi Rift: The influence of inherited lithospheric heterogeneity and kinematics in the evolution of continental rifts, *Tectonics, 34*, 2399–2417.

Leseane, K., E. A. Atekwana, K. L. Mickus, M. G. Abdelsalam, E. M. Shemang, and E. A. Atekwana (2015), Thermal perturbations beneath the incipient Okavango Rift Zone, northwest Botswana, *J. Geoph. Res*., *120*, 1210-1228.

Ma, G. Q., X. J. Du, L. L. Li, and L. S. Meng (2012), Interpretation of magnetic anomalies by horizontal and vertical derivatives of the analytic signal, *Appl. Geoph.*, *9*(4), 468-474.

Macheyeki, A. S., H. Mdala, L. S. Chapola, V. J. Manhiça, J. Chisambi, P. Feitio, A. Ayele, J. Barongo, R. W. Ferdinand, G. Ogubazghi, and B. Goitom (2015), Active fault mapping in Karonga-Malawi after the December 19, 2009 Ms 6.2 seismic event, *J. of Afr. Earth Sci.*, *102*, 233-246.

McCartney, T., and C. A. Scholz (2016), A 1.3 million year record of synchronous faulting in the hanging wall and border fault of a half-graben in the Malawi (Nyasa) Rift, *J. Struct. Geol*., *91*, 114-129.

Miller, H. G., and V. Singh (1994), Semiquantitative techniques for the removal of directional trends from potential field data, *J. Appl. Geoph*., *32*, 199-211.

Modisi, M. P., E. A. Atekwana, A. B. Kampunzu, and T. H. Ngwisanyi (2000), Rift kinematics during the incipient stages of continental extension: evidence from the nascent Okavango rift basin, northwest Botswana, *Geology*, 102, 363-376.

Morley, C. K. (1995), Developments in the structural geology of rifts over the last decade and their impact on hydrocarbon exploration, *Geol. Soc., London, Special Publications*, *80*(1), 1-32.

Morley, C. K. (2010), Stress re-orientation along zones of weak fabrics in rifts: An explanation for pure extension in 'oblique' rift segments?, *Earth and Planet. Sci. Lett.*, *297*(3), 667-673.

Morley, C. K., C. Haranya, W. Phoosongsee, S. Pongwapee, A. Kornsawan, and N. Wonganan (2004), Activation of rift oblique and rift parallel pre-existing fabrics

during extension and their effect on deformation style: examples from the rifts of Thailand, *J. Struct. Geol.*, *26*(10), 1803-1829.

Mortimer, E., D. A. Paton, C. A. Scholz, M. R. Strecker, and P. Blisniuk (2007), Orthogonal to oblique rifting: effect of rift basin orientation in the evolution of the North basin, Malawi Rift, East Africa, *Basin Res.*, *19*(3), 393-407.

Mortimer, E.J., D. A. Paton, C. A. Scholz and M. R. Strecker (2016a), Implications of structural inheritance in oblique rift zones for basin compartmentalization: Nkhata Basin, Malawi Rift (EARS), *Mar. Petrol. Geol*., *72*, 110-121.

Mortimer, E., L. A. Kirstein, F. M. Stuart, and M. R. Strecker (2016b), Spatio-temporal trends in normal-fault segmentation recorded by low-temperature thermochronology: Livingstone fault scarp, Malawi Rift, East African Rift System, *Ear. Plan. Sci. Lett.*, *455*, 62-72.

Moussa, H. H. M. (2008), Spectral P-wave magnitudes, magnitude spectra and other source parameters for the 1990 southern Sudan and the 2005 Lake Tanganyika earthquakes, *J. Afr. Earth Sci*., *52*(3), 89-96.

Muirhead, J. D., S. A. Kattenhorn, H. Lee, S. Mana, B. D. Turrin, T. P. Fischer, G. Kianji, E. Dindi, and D. S. Stamps (2016), Evolution of upper crustal faulting assisted by magmatic volatile release during early-stage continental rift development in the East African Rift, *Geosphere, 12*(6), 1670-1700.

Oliva S. J. C., C. J. Ebinger, D. Keir, D. J Shillington, and P. R. N. Chindandali (2016), Deciphering the role of fluids in early stage rifting from full moment tensor

inversion of East African earthquakes, *American Geophysical Union (AGU) 2016 meeting* poster T51C-2942.

Phillips, T. B., C. A. Jackson, R. E. Bell, O. B. Duffy, and H. Fossen (2016), Reactivation of intrabasement structures during rifting: A case study from offshore southern Norway, *J. of Struc. Geol.*, *91*, 54-73.

Ring, U. (1993), Aspects of the kinematic history and mechanisms of superposition of the Proterozoic mobile belts of eastern Central Africa (northern Malawi and southern Tanzania), *Precambrian Res.*, *62*(3), 207-226.

Ring, U. (1994), The influence of preexisting structure on the evolution of Cenozoic Malawi Rift (East African Rift System), *Tectonics*, *13*(2), 313-326.

Ring, U., A. Kröner, R. Buchwaldt, T. Toulkeridis, and P. W. Layer (2002), Shear-zone patterns and eclogite-facies metamorphism in the Mozambique belt of northern Malawi, east-central Africa: implications for the assembly of Gondwana, *Precambrian Res.*, *116*(1), 19-56.

Ring, U., H. L. Schwartz, T. G. Bromage, and C. Sanaane (2005), Kinematic and sedimentological evolution of the Manyara Rift in northern Tanzania, East Africa, *Geol. Magazine*, *142*(04), 355-368.

Rosendahl, B. R. (1987), Architecture of continental rifts with special reference to East Africa, *Annu. Rev. Earth Planet. Sci.*, *15*, 445-503.

Rosendahl, B. R., D. J. Reynolds, P. M. Lorber, C. F. Burgess, J. McGill, D. Scott, J. J. Lambiase, and S. J. Derksen (1986), Structural expressions of rifting: lessons from Lake Tanganyika, Africa, *Geol. Soc., London, Spec. Pub., 25*(1), 29-43.

Salem, A., S. Williams, J. D. Fairhead, R. Smith and D. Ravat (2007), Interpretation of magnetic data using tilt-angle derivatives, *Geophysics*, *73*(1), L1–L10.

Saria, E., E. Calais, D. S. Stamps, D. Delvaux, and C. J. H. Hartnady (2014), Present-day kinematics of the East African Rift, *J. Geoph. Res.*: *Solid Earth*, *119*(4), 3584-3600.

Schlische, R. W. (1991), Half-graben basin filling models: new constraints on continental extensional basin development, *Basin Res.*, *3*(3), 123-141.

Schrenk, F., T. G. Bromage, C. G. Betzler, U. Ring, and Y. M. Juwayeyi (1993), Oldest Homo and Pliocene biogeography of the Malawi rift, *Nature*, *365*, 833-836.

Seismological Bulletin of Malawi (2015), Malawi Geological Survey, Zomba, Malawi.

Seyitoglu, G., O. Tekeli, I. Çemen, S. Sen, and V. Isik (2002), The role of the flexural rotation/rolling hinge model in the tectonic evolution of the Alasehir graben, western Turkey, *Geol. Magazine, 139*(01), 15-26.

Smith, R. S., and A. Salem (2005), Imaging depth, structural and susceptibility from magnetic data: The advanced source parameter imaging method, *Geophys. 70*(4), L31-L38.

Smith, R. S., J. B. Thurston, T. F. Dai, and I. N. MacLeod (1998), iSPITM—the improved source parameter imaging method, *Geoph. Prosp.*, *46*(2), 141-151.

Stamps, D. S., E. Calais, E. Saria, C. Hartnady, J.-M. Nocquet, C. J. Ebinger, and R. M. Fernandes (2008), A kinematic model for the East African Rift, *Geoph. Res. Lett*., *35*, L05304.

Versfelt, J., and B. Rosendahl (1989), Relationship between pre-rift structure and rift architecture in Lakes Tanganyika and Malawi, East Africa, *Nature*, 337, 354-357.

Wells, D. L. and K. J. Coppersmith (1994), New empirical relationships among magnitude, rupture length, rupture width, rupture area, and surface displacement, *Bull. Seis. Soc. Amer.*, *84*(4), 974-1002.

Wheeler, W., and J. Karson (1989), Structure and kinematics of the Livingstone Mountains border fault zone, Nyasa (Malawi) Rift, southwestern Tanzania, *J. Afric. Earth Sci. (and Mid. East)*, *8*, 393–413.

Wilson, R. W., R. E. Holdsworth, L. E. Wild, K. J. W. McCaffrey, R. W. England, J. Imber, and R. A. Strachan (2010), Basement-influenced rifting and basin development: A reappraisal of post-Caledonian faulting patterns from the North Coast Transfer Zone, Scotland, *Geol. Soc., London, Special Publications*, *335*(1), 795-826.

Withjack, M. O., R. W. Schlische, and P. E. Olsen (2002), Rift-basin structure and its influence on sedimentary systems. Sedimentation in Continental Rifts, *SEPM Spec. Pub., 73*, 57–81.

Wright, T.J., C. Ebinger, J. Biggs, A. Ayele, G. Yirgu, D. Keir, and A. Stork (2006), Magma-maintained rift segmentation at continental rupture in the 2005 Afar dyking episode, *Nature*, *442*(7100), 291-294.

Zang, A., and O. Stephansson (2010), Stress Field of the Earth's Crust, *Springer, New York*.

# CHAPTER II

# ELECTRICAL RESISTIVITY AND TEMPORAL AEROMAGNETIC IMAGING OF THE 2009 KARONGA, MALAWI EARTHQUAKE CAUSATIVE FAULT AND RUPTURE ZONE

F. Kolawole[1], E. A. Atekwana[1], D. A. Laó-Dávila[1], M. G. Abdelsalam[1], T. Ivey[1], P. R. Chindandali[2], J. Salima[2], and L. Kalindikafe[3]

[1]Oklahoma State University Main Campus, Stillwater, OK, United States

[2]Geological Survey of Malawi, Zomba, Malawi

[3]Malawi University of Science and Technology, Malawi

Corresponding author: Estella Atekwana (estella.atekwana@okstate.edu)

## SUMMARY

The 2009 Karonga, Malawi earthquake caused a surface rupture length of 14-18 km along a single W-dipping fault within the unconsolidated coastal plain sediments on the western shores of the northern part of Lake Malawi. Although the earthquake damage zone is characterized by surface ruptures and liquefaction sand blows, the origin of the causative fault and the near-surface structure of the damage zone are not known. We used pre- and post-earthquake aeromagnetic data and surface rupture locations to investigate the origin of the causative fault, and integrated our results with electrical resistivity tomography to

elucidate the shallow-subsurface (<100 m) structure of the earthquake rupture zone. We applied mathematical derivative filters to the aeromagnetic data to enhance basement structures underlying the rupture zone and surrounding areas, and acquired two-dimensional (2-D) electrical resistivity tomography (ERT) profiles along and across the rupture zone. The earthquake surface ruptures align with a distinct NNW-striking magnetic lineament defining a west-dipping normal fault on filtered pre- and post-aeromagnetic maps. We also observe that the surface ruptures only cover about half (16.4 km) of the total length of the magnetic lineament (37 km). Inverted ERT profiles reveal three regional geoelectric layers in which the topmost layer is a 15 m-thick interval of thin, lens-shaped discontinuous zones of high and low resistivity values. The underlying second geoelectric layer is characterized by a 27 m-thick zone of very high electrical resistivity (30-100 Ωm), and the basal geoelectric layer extends downwards from 42 m depth and is characterized by extremely low resistivity values (1.0-6.0 Ωm). The lateral continuity of the geoelectrical layering is truncated by a zone of electrical disturbance (electrical mélange) which coincides with areas of surface rupturing along the causative fault. Analyses of our data show that the 2009 Karonga earthquake was associated with the partial rupture of a pre-existing basement fault, dubbed the St. Mary Fault (SMF). We also present for the first time, the seismotectonic map of the Karonga area. ERT profiles reveal the near-surface emplacement and preservation of sand dike and soil liquefaction structures within the 'electrical mélange', along with buried faults in the shallow subsurface interpreted as relics of previous earthquake events along the SMF. We suggest that the presence of preserved

near-surface lenses of liquefied sand pose potential hazard in the event of a future earthquake in the area. Our study demonstrates that the integration of electrical resistivity tomography and aeromagnetic data can be very useful in seismic hazard analysis.

**Key words:** Seismicity and tectonics; Fractures and faults; Paleoseismology; Earthquake hazards; Magnetic anomalies: modelling and interpretation; Electrical resistivity tomography (ERT).

## 1 INTRODUCTION

The East African Rift (EARS; Fig. 1 inset) is the largest seismically active continental rift system on Earth today, in which shallower seismicity (<15 km) is mostly associated with strain localization within the rift axis (Craig *et al*. 2011; Kearey *et al*. 2009). The Rukwa-Malawi Rift zone, located along the southern branch of the EARS, recorded the largest historically documented earthquake in Africa which featured an $M_s$ 7.4 earthquake in 1910 (Ambraseys & Adams, 1991). Due to the characteristic large seismogenic thickness (>30 km), mature fault systems shown by long fault scarps (~100 km), and slow strain rates (2.2 mm/year) of the Malawi Rift, it has been suggested that this segment of the EARS is capable of hosting infrequent seismic events of up to $M_w$ 7.0 or larger (Ebinger *et al.* 1987, 1993; Jackson & Blenkinsop 1997; Saria *et al*. 2014; Hodge *et al*. 2015). Within the past few years, the North Basin of Malawi Rift has been affected by two moderate - strong

earthquakes namely the 2009 $M_w$ 6.0 Karonga earthquake swarm and the 2014 $M_w$ 5.1 Karonga earthquake sequence. Kolawole *et al*. (2016) showed that the clustering of seismicity on the western part of the North Basin half-graben is associated with active deformation of the hinge zone of the half-graben, facilitated by the presence of favorably-oriented pre-existing basement fabric.

Between December 6th and 19th, 2009, the Karonga area of the North Basin, located on the western shores of Northern Lake Malawi was affected by a swarm of earthquakes. The seismic events include seven $M_w$ 4.9-6.0 events and a series of $M_b \leq 4.6$ earthquakes recorded for another month after the larger events (Fig. 1; Biggs *et al*. 2010; Hamiel *et al*. 2012). The earthquake resulted in multiple fatalities, hundreds of injuries and the damage of thousands of buildings (Hamiel *et al*. 2012; Goda *et al*. 2016). The earthquake events which occurred at <8 km centroid depths were accompanied by coseismic surface ruptures with up to 60 cm vertical displacements and several liquefaction-induced sand blows within the surficial coastal plain sediments (Figs 2a to f). Field mapping of surface ruptures and Differential Interferometric Synthetic Aperture Radar (InSAR) modeling of the surface deformation associated with the coseismic events showed that the earthquake was associated with the rupture of a shallow, single NNW-SSE striking and SW-dipping normal fault (Biggs *et al.* 2010; Hamiel *et al*. 2012). Hamiel *et al*. (2012) and Macheyeki *et al*. (2015) documented cumulative surface rupture length of 14.3 - 18 km. Based on the spatial distribution and trend of the earthquake surface ruptures, Macheyeki *et al.* (2015) suggested that the fault that ruptured during the earthquake has three segments with ~1.6

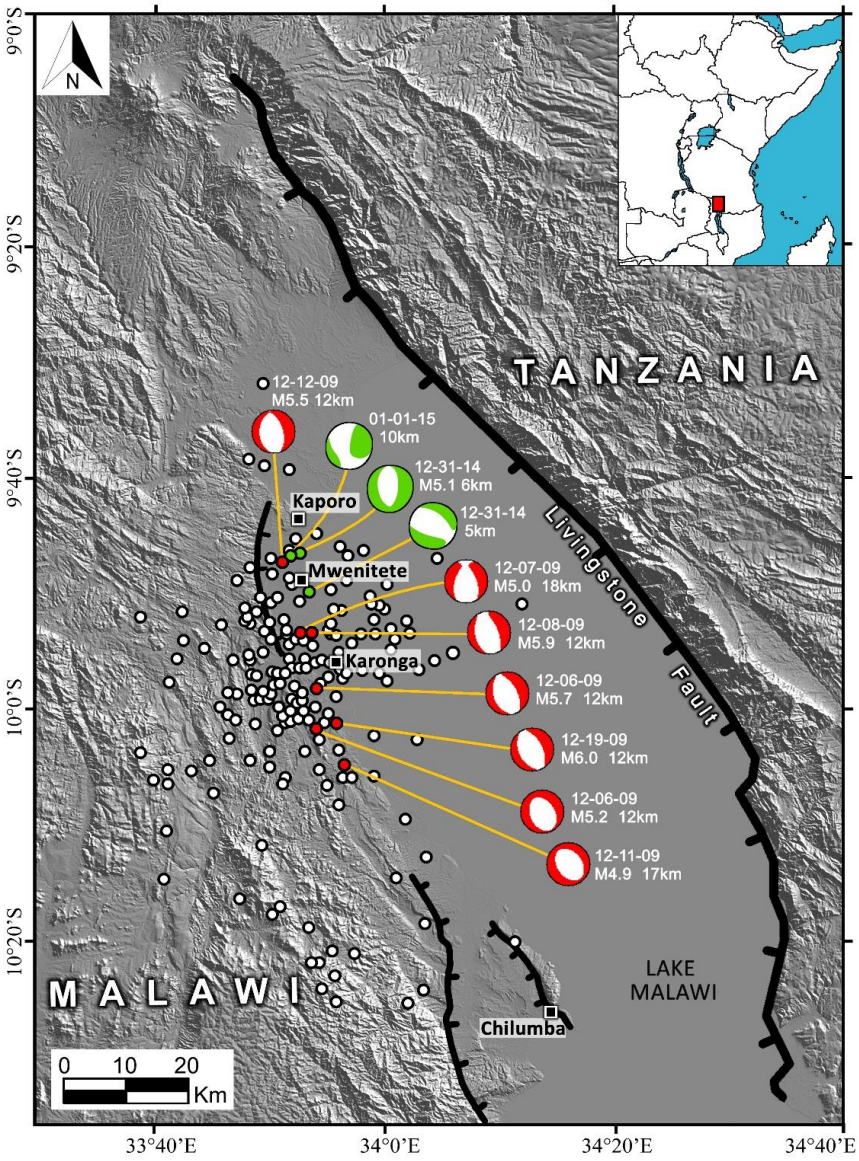


**Figure 1.** Shuttle Radar Topography Mission (SRTM) Digital Elevation Model (DEM) of northern Malawi showing major rift-related morpho-tectonic features and location of earthquakes associated with the 2009 Karonga earthquake swarm (Red circles = $M_w \geq 4.9$ earthquakes, white circles = $M_w \leq 4.9$) and the 2014 Karonga earthquake sequence (green circles). The 2009 earthquake data were obtained from the Geological Survey Department of Malawi and focal plane solutions from Global Centroid Moment Tensor database. The 2014 earthquake epicenter locations were obtained from Oliva *et a*l. (2016). Inset map shows map of Eastern Africa and the location of northern Malawi (red box).

km gap along-strike of the southern segment of the fault. The local people named the ruptured fault “St. Mary Fault”.

The 2014 $M_w$ 5.1 Karonga earthquake sequence occurred between 31st December, 2014 and 1st January, 2015 and their epicenters were located at ~15 km north of Karonga town (Fig. 1). During this period, three $M_w$ 5.1 seismic events with hypocentral locations at 5-10 km depths were recorded by the SEGMeNT (Study of Extension and maGmatism in Malawi aNd Tanzania) array (Oliva *et al.* 2016). The focal plane mechanism solutions for the earthquake sequence indicate normal and normal-oblique faulting on N-S and NNW-SSE –oriented planes. There has been no reports of coseismic surface ruptures associated with this earthquake event.

Since the ruptured fault(s) associated with these earthquakes had no known surface expression before the earthquake events, the origin of the seismogenic fault(s) is not known, and it is not clear whether the rupture created a new fault or occurred on a pre-existing fault. Prior to our study, there exists no information on subsurface faults or paleoseismicity within this seismogenic Karonga area of the Malawi Rift. Therefore, there is additional need to characterize the buried fault segments in the area in terms of location, geometry, length, subsurface setting, short- and long-term slip history, seismic behavior and associated seismic hazard. In this study, we provide new data useful in defining the crystalline basement and near-surface structural setting and framework for the Karonga area of the North Basin.


**Figure 3.** Photographs showing coseismic surface deformation associated with the ruptured fault of the 2009 Karonga earthquake. (a - b) Coseismic surface ruptures with normal-faulting style of displacement. HW = hanging wall, FW = foot wall. (c) Coseismic surface rupture with 13 cm lateral opening and 9 cm vertical offset. (d) Coseismic surface ruptures with sand blows.

We use temporal aeromagnetic data to image crystalline basement faults and high-resolution electrical resistivity tomography to image the near-surface structure of the rupture zone of the St. Mary Fault (SMF). We then determine the spatial correlation between basement-rooted faults on pre- and post-earthquake data and the locations and trend of the earthquake surface ruptures in order to determine the origin, geometry and seismic hazard of the causative fault(s). In addition, we determine the spatial correlation between the surface ruptures and the near-surface electrical signatures along the strike of the SMF in order to investigate paleoseismicity along the fault. We also present one of the first results of geoelectrical imaging of an earthquake rupture zone with associated liquefaction structures.

## 2 GEOLOGICAL SETTING

The study area (herein referred to as the Karonga area), is located on the shoaling side of the North Basin half-graben. The North Basin half-graben, which constitutes the northernmost segment of the Malawi Rift, is bounded on the east by the 100 km-long, NW-striking and steeply SW-dipping Livingstone border fault (Wheeler & Karson, 1989; Figs 1 and 3). The hanging wall block of the fault has been deformed by numerous NW-striking intrabasin normal faults found under that waters of Lake Malawi (Nyassa). Most of these intrabasinal faults are synthetic to the Livingstone Fault (Ring, 1994; Mortimer *et al*. 2007). The basin fill is composed of Neogene-Quaternary Chiwondo and Chitimwe lacustrine sediments which overlie Precambrian igneous and metamorphic rocks (Fig. 3; Schrenk *et*

*al*. 1993; Ring, 1994). The sedimentary rocks are covered by Quaternary coastal plain alluvial sediments composed of sandy clays, terrace sands, and gravels (Macheyeki *et al*. 2015). In the Karonga area, the alluvium and sedimentary rocks are underlain by crystalline basement rocks of the Precambrian Mughese Shear Zone (MSZ) which consist of sheared amphibolite, gneisses and granites (Ring *et al*. 2002; Ring, 1994).

West of Karonga town, the extent of the basin is delimited by the N-S –striking, east-dipping Karonga Fault. In the Karonga area, within the coastal plain of Lake Malawi, there is little or no topographic variation, and prior to this study, there was no information on the structural characteristics of the subsurface. Using Global Positioning System (GPS) and earthquake slip vectors rigid plate model, Saria *et al.* (2014) estimated a rift opening rate of 2.2 mm/year and suggested an E-W present-day extension direction for the northern Malawi Rift.

## 3 DATA AND METHODS

### 3.1 Aeromagnetic data

In this study, we used two vintages of aeromagnetic data which cover the Karonga area, consisting of a 1984-1985 vintage (pre-earthquake) and 2013 vintage (post-earthquake). We obtained the 1984-1985 aeromagnetic data from the Aeromagnetic Map of Malawi (1985), which was acquired with a 120 m flight elevation along NE–SW lines with spacing of 1 km and tie-line spacing of 10 km. The 2013 aeromagnetic data, provided by the Geological Survey of Malawi, was acquired with a flight elevation of 80 m along NE–SW

lines spaced at 250 m, NW–SE -oriented tie lines spaced 5 km apart. The pre- and post-earthquake residual magnetic field data were reduced to pole (RTP) (Baranov, 1957*;* Arkani-Hamed, 1988) in order to remove the skewness of the anomalies and directly position magnetic anomalies over their sources. In order to enhance magnetic gradients associated with normal faults within the basement, we applied vertical (Dz) and horizontal derivative (Dx and Dy) filters to the aeromagnetic grids. Processing and filtering of aeromagnetic data were done using Geosoft's Oasis Montaj software.

### 3.2 Earthquake surface ruptures

In order to identify the surface expression and extents of the 2009 Karonga Earthquake shatter zone, we obtained a total of 408 coordinates of surface deformation (surface rupture and sand blow) locations previously published data on the earthquake. This data includes 396 surface rupture and sand blow location coordinates from Macheyeki *et al*. (2015), 8 surface rupture locations were obtained from Hamiel *et al*. (2012), and based on our communication with the locals during our field visit, we documented 4 additional surface rupture and sand blow locations.

### 3.3 Electrical resistivity tomography (ERT)

We acquired electrical resistivity data in July 2015 (6 years after the earthquake), along three transects (Figs 4a to c) using an Iris Syscal Pro 10-channel resistivity meter, 72 electrodes and 10 m electrode spacing. We adopted the dipole–dipole array to effectively

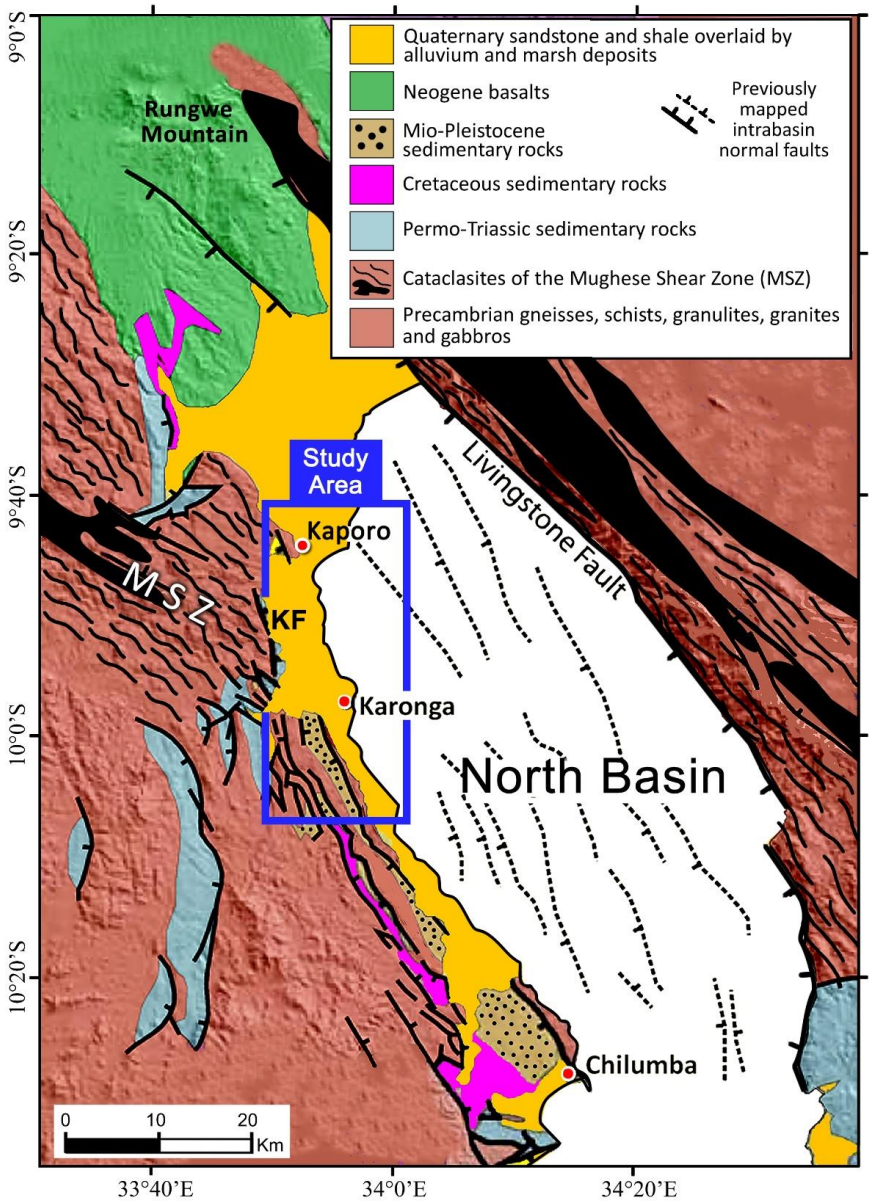


**Figure 3.** Geological map of the northern Malawi, covering the North Basin of the Malawi Rift and surrounding basement rocks (modified after Wheeler and Karson, 1989; and Biggs *et al.* 2010). MSZ = Mughese Shear Zone (Precambrian), KF = Karonga fault. The Karonga area is enclosed in blue box.

map vertical structures associated with the near surface propagation of the SMF due to its very high sensitivity to horizontal changes in resistivity (Loke, 2001). Profile-1 was 1070 m long, oriented NW-SE, and extended from unruptured to ruptured segments of the fault (Fig. 4b). Profile-2 and profile-3 were 710 m long. Profile-2 was oriented ENE-WSW and profile-3 was oriented WNW-ESE, both roughly orthogonal to the trend of the rupture zone at the locations (Figs 4b and c). We processed and inverted the acquired data with the RES2DINV software using the finite-element approach and a Gauss-Newton algorithm (Loke & Barker, 1996). There were no bore hole lithostratigraphic information near the study site for lithologic calibration of the profiles, and the inversion profiles were also not corrected for topography because of insignificant elevation variation along the survey transects.

## 4 RESULTS

### 4.1 Filtered aeromagnetic data

Figs 5(a) and (b) show vertical derivative maps of the RTP pre- (1984-1985) and post-earthquake (2013) aeromagnetic grids. The overall trend of magnetic lineaments on both aeromagnetic map vintages are consistent, evidenced by the overall NNW-SSE trend of the magnetic lineaments. The magnetic fabric of the MSZ outcrop exposures is characterized by high frequency, short wavelength magnetic lineaments ("MSZ" in Fig. 5). In the Karonga area, where basement rocks are buried beneath ~350-500 m overburden of sedimentary rocks (Kolawole *et al*. 2016), we identify distinct magnetic lineaments that

strike 148°-162° (NNW-SSE) and interpret them as magnetic gradients associated with basement-rooted normal faults buried beneath the coastal plain alluvium and sedimentary rocks. These magnetic lineaments are characterized by a gradient that is steeper on their western flank than on their eastern flank; which indicate that the normal faults dip to the southwest and they bound faulted basement blocks that tilt to the east (Fig. 6).

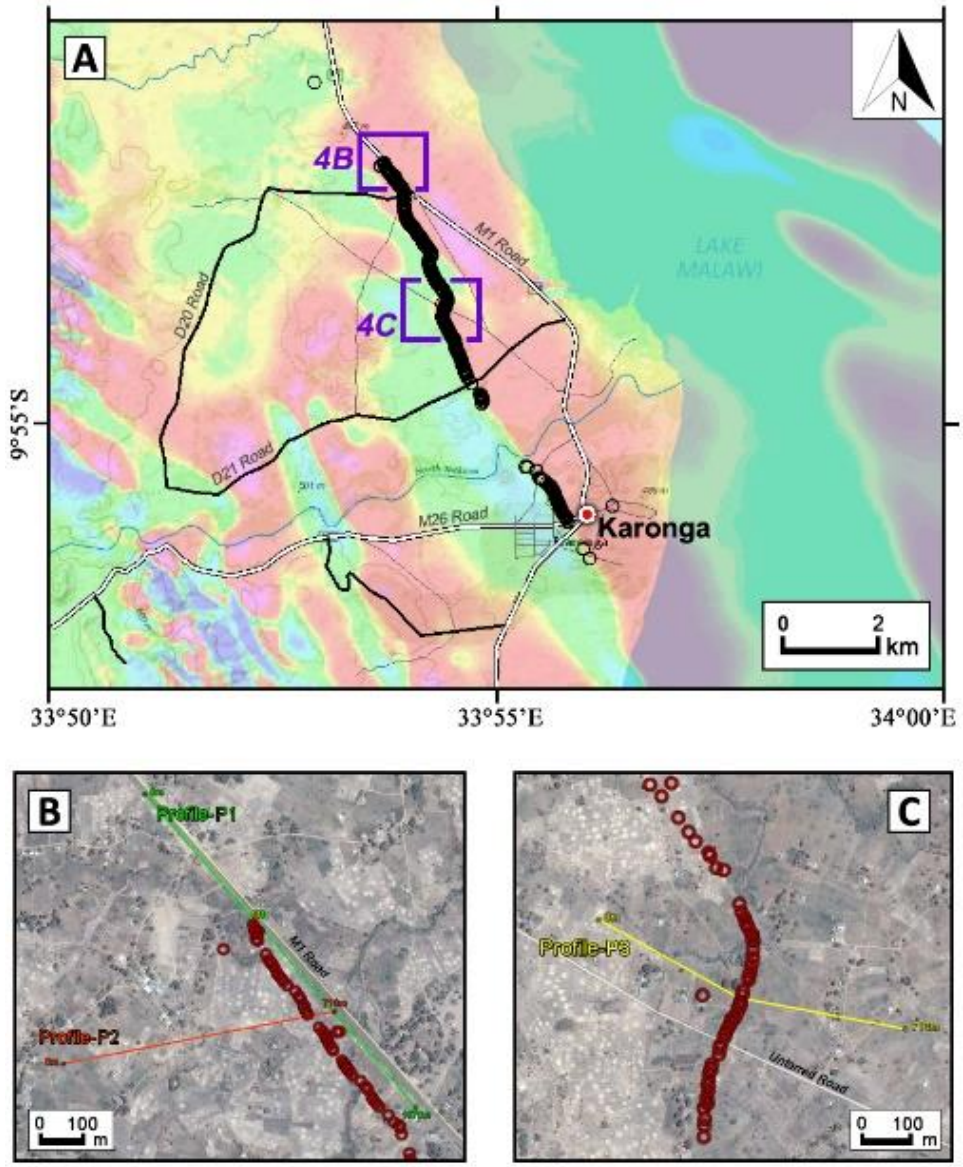


**Figure 4.** (a) First vertical derivative of the reduced to pole (RTP) grid of aeromagnetic map draped on the contour and base map of Karonga showing the location of the electrical resistivity survey transects used in this study and mapped locations of surface ruptures (black circles) along the edge of the St. Mary Fault magnetic lineament. (b - c) Aerial view of electrical resistivity tomography survey sites showing transects for electrical resistivity tomography Profile-P1 along the rupture zone, and Profile-P2 and P3 across the rupture zone. Red circles represent surface ruptures.

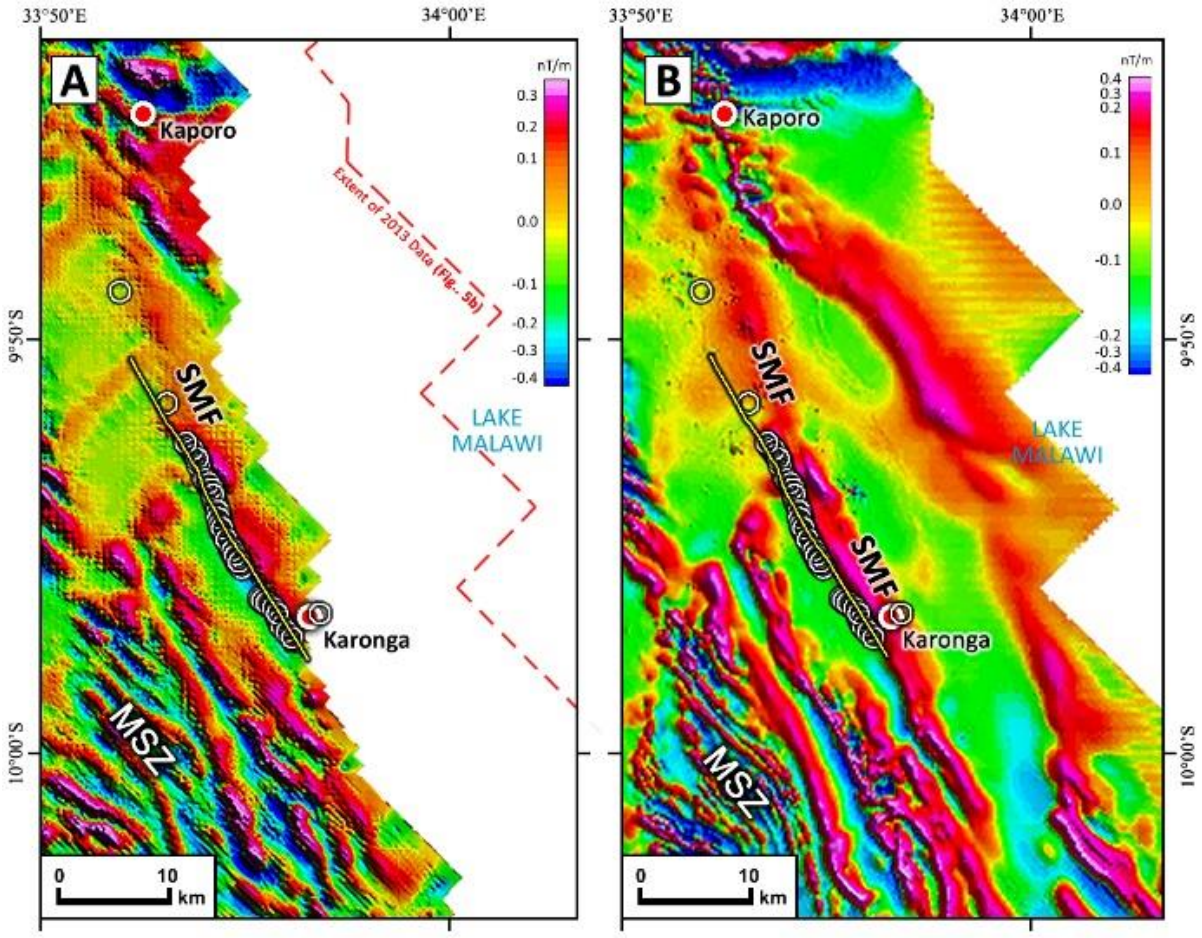


**Figure 5.** First vertical derivative of the reduced to pole (RTP) grid of the (a) pre-earthquake 1984/1985 aeromagnetic map and (b) 2013 aeromagnetic map of Karonga area. The maps show the correlation between previously published InSAR fault-trace models for the 2009 Karonga earthquake (from Biggs *et al.* 2010 and Hamiel *et al.* 2012) (yellow line), mapped locations of the earthquake surface ruptures (white circles) and a prominent NNW-SSE -striking magnetic lineament in the basement.

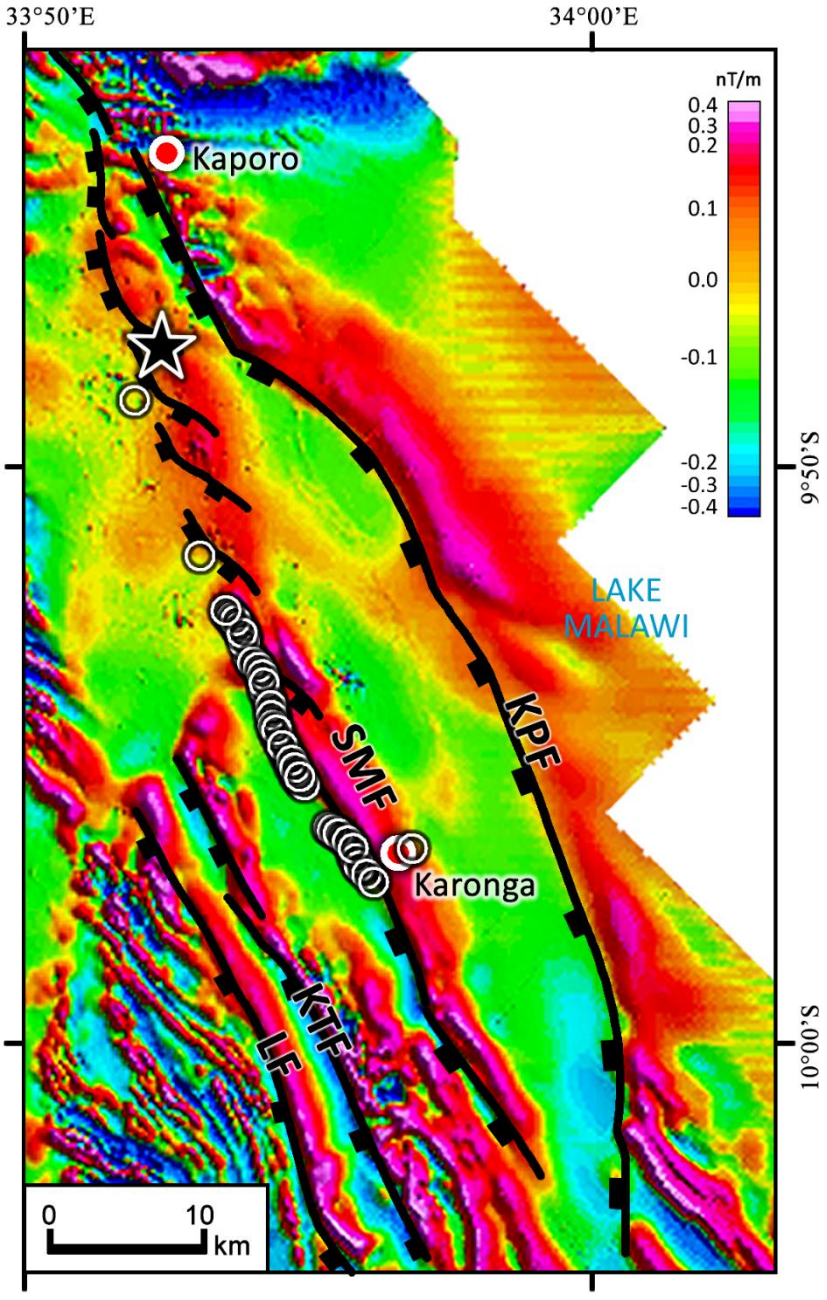


**Figure 6.** First vertical derivative of the reduced to pole (RTP) grid of the 2013 aeromagnetic map of Karonga area with fault interpretations. White circles = surface rupture locations, KPF = Kaporo Fault, KTF = Katesula Fault, LF = Lupaso Fault, SMF = St. Mary Fault. Black star = Epicenter of 2014 Karonga earthquake sequence (from Oliva *et al.* 2016).

### 4.2 Distribution of earthquake surface deformation locations

The surface deformation locations of the 2009 Karonga earthquake describe a NNW-SSE trend and extend over a total length of 16.4 km (Fig. 5b). Figs 5(a) and (b) also show an overlay of the surface deformation locations on vertical derivative maps of the pre- and post-earthquake aeromagnetic grids. The mapped surface deformation locations align with a distinct magnetic lineament that is clearly observable on both the 1984-1985 and 2013 aeromagnetic maps. The surface deformation locations only cover about half the length of the magnetic lineament with which they align which extends over a total length of 37 km (Fig. 5b). We also observe that 99% of the surface deformation locations appear to cluster along the central segment of the magnetic lineament. We interpret this magnetic lineament as a NNW-SSE –striking, E-dipping basement-rooted normal fault, which we herein refer to as the St. Mary Fault (SMF).

### 4.3 ERT data

Profile P1 was acquired along the SMF and the northwestern-half of this profile extends along the segment of the fault that does not show earthquake surface deformation, whereas, its southeastern-half extends into the ruptured fault segment (Fig. 4b). Profiles P2 and P3 extend almost orthogonal across the SMF (Figs 4b and c). The inversion of the electrical resistivity data of Profiles P1, P2 and P3 (Figs 7a-d, and Figs 8a-d) reveal three main geoelectric layers. The topmost layer is ~15 m thick, composed of thin, lens-shaped, discontinuous zones of high and low resistivity values (15 - 60 Ωm). The second geoelectric

layer is ~27 m thick and is characterized by the highest resistivity values (30 - 100 Ωm) observed at the site. The third geoelectric layer is characterized by the lowest resistivity values at the site, ranging between 1.0 and 6.0 Ωm, and extends from 42 m depth downward into the subsurface. Along Profile P1, the second geoelectric layer is truncated at electrode location 440 m by a 60-80 m wide vertical medium-resistivity (~14 Ωm) structure. To the southeast of this structure, the geoelectrical layering is disturbed resulting in a heterogeneous mixture of high and low resistivity values herein referred to as an "electrical mélange". Profiles P2 and P3 also show truncation and disruption of layer 2 at locations coincident with surface ruptures, although the disruption is to a lesser extent. Along Profile P3 for example, a localized region of lower resistivity values characterizes the ruptured zone.

## 5 DISCUSSION

### 5.1 Origin of the ruptured fault and seismotectonic framework of the Karonga area

As shown in Fig. 5b the mapped surface deformation locations align along a distinct 37 km long, NNW-SSE –striking, SW-dipping basement-rooted fault. The coincidence of the surface rupture locations with the edge of the same distinct magnetic lineament on the pre- and post-earthquake filtered RTP aeromagnetic data (Figs 5a and b) suggests that the 2009 Karonga earthquake is associated with the rupture of a pre-existing buried basement fault called the St. Mary Fault (SMF). The SMF is synthetic to the Livingstone Fault (the border fault of the North Basin) and its location, strike and southwest dip direction as

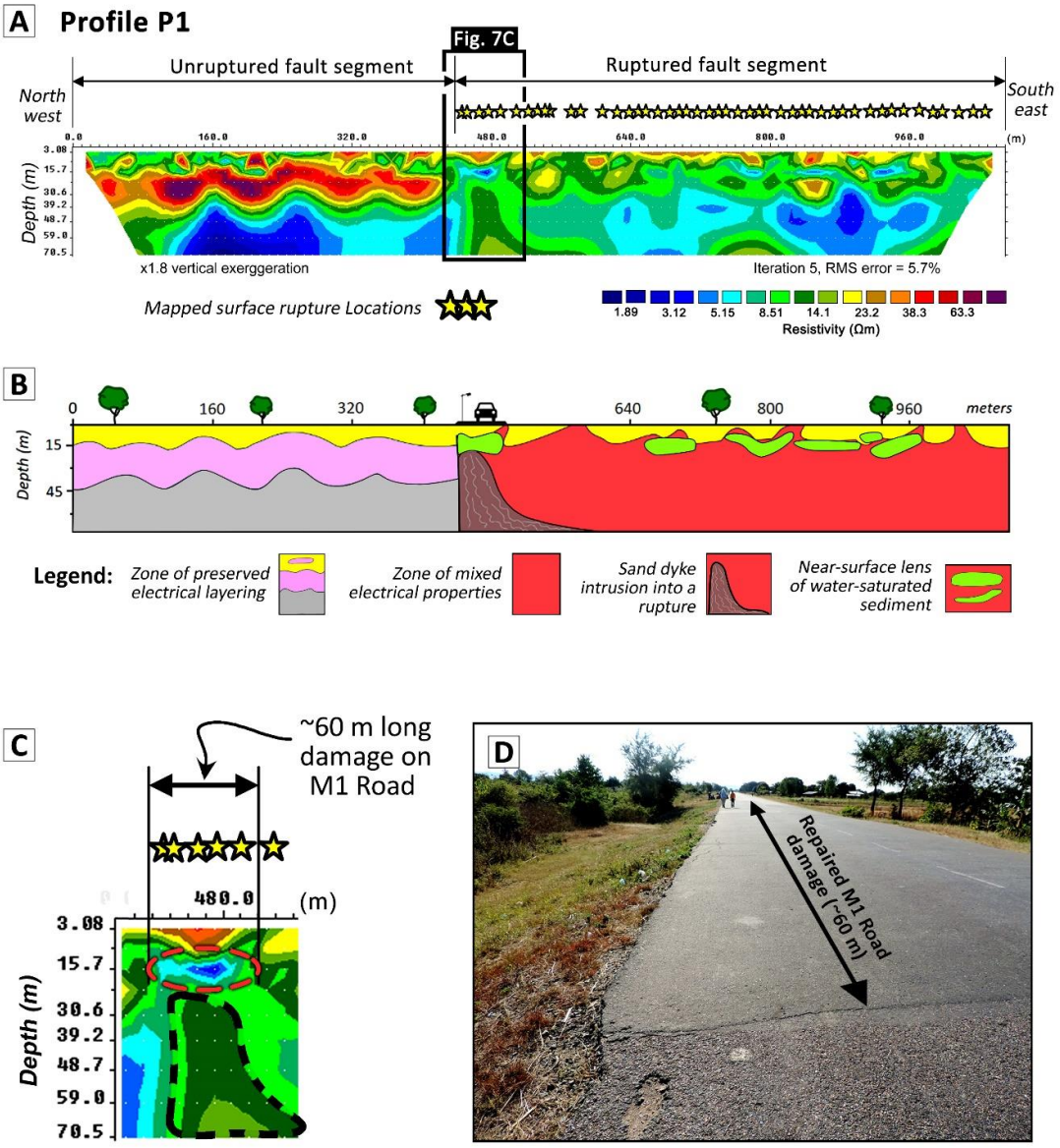


**Figure 7.** (a) Inverted electrical resistivity profile for Profile P1 (along the rupture zone). (b) Interpretation of the electrical resistivity inversion for Profile P1. (c) Close-up and interpretation of the electrical structure beneath the ruptured segment of M1 road. (d) Photograph showing repaired ruptured segment of the M1 road.

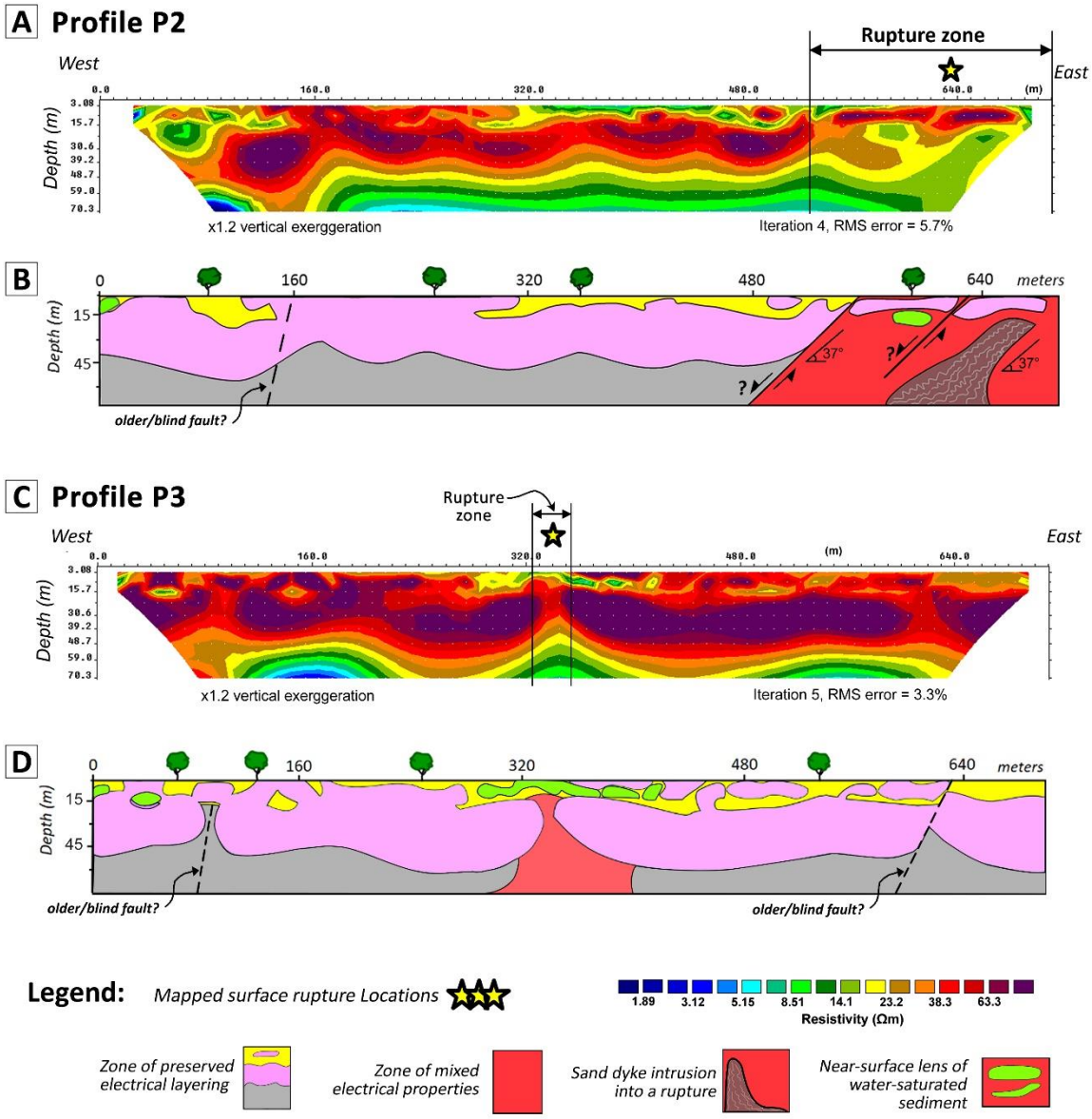


**Figure 8.** (a) Inverted electrical resistivity profile for Profile P2 (across the rupture zone). (b) Interpretation of the electrical resistivity inversion for Profile P2. (c) Inverted electrical resistivity profile for Profile P3 (across the rupture zone, farther south of Profile P2). (b) Interpretation of the electrical resistivity inversion for Profile P3.

revealed by the filtered aeromagnetic maps is consistent with the results of the DInSAR studies on the 2009 Karonga earthquake by Biggs *et al.* (2010) and Hamiel *et al.* (2012).

Fig. 5b shows that the surface deformation locations occur only along the central part of the SMF and cover only about half of the total length of the fault, which suggests that the 2009 seismic event was associated with the partial rupture of the SMF. We suggest that the unruptured parts of the SMF may be loaded and could rupture in the future. The occurrence of the $M_w$ 5.1 2014 Karonga earthquake along the SMF at ~17 km NNW of Karonga town (Oliva *et al.* 2016) (Black start on Fig. 6) supports our proposed seismic hazard of the unruptured segments of the SMF. Within the coastal plain sediments of Lake Malawi, we have also identified other buried basement-rooted faults with the similar strike, dip direction and style of fault slip (normal) as the SMF (Fig. 6). These are the Kaporo Fault (KPF), Katesula Fault (KTF) and Lupaso Fault (LF).

### 5.2 Near-surface structure of earthquake rupture zone

The delineated structural framework of the SMF identified from filtered RTP aeromagnetic map provides a backdrop for characterizing of the near-surface structure of the earthquake rupture zone. The truncation of the regional electrical layering by the geoelectrical mélange observable on Profile P1 along the SMF (Figs 7a and b) confirms that only parts of the fault ruptured during the 2009 Karonga Earthquake. Along the SMF, the rupture zone is at least 180 m wide at the northern termination of the surface ruptures

(Profile P2; Figs 8a and b), but narrower (≤40 m) farther south (Profile P3; Figs 8c and d); this suggests possible northward continuation of the rupture at depth in the subsurface. This observation is consistent with Macheyeki *et al*. (2015) observation of a general southward tapering of mean vertical offset and fracture width along the trend of the surface ruptures.

We observe that the dominance of unconsolidated Quaternary beach sands, alluvium and marsh deposits in the surficial geology of the Karonga area (Fig. 2) provided a suitable geologic setting for coseismic liquefaction during the 2009 earthquake event. We interpret the vertical, moderately resistive structure that sits at the contact between the electrical mélange and regional electrical layering (Figs 7a to c) as a localized fine-grained, possibly low porosity sand dike intrusion. This structure is overlain by a ~60 m lens of water-saturated sediments which we interpret to have developed and was emplaced in the near-surface during earthquake liquefaction and are coincident with locations of sand blows along the surface ruptures. Incidentally, the width of the water saturated lens is consistent with the width of a portion of the M1 road that was damaged during the earthquake (Figs 7c and d). Other examples of coseismic liquefaction sand blows along the 2009 Karonga earthquake surface ruptures are shown in Fig. 3. The vertical extent of the sand dike indicates that the liquefied sediments came from depths greater than 70 m (Fig. 7c). These lenses of highly conductive material can be observed beneath zones of surface rupturing along the SMF on all the profiles and are located at a common depth of 15 to16 m. Profiles P1 and P3 show spectacular examples of the saturated sediments underlying the earthquake rupture zone (Figs 7b and 8d). We propose that the upward transport of

fine-grained sediments and groundwater through the rupture zone created isolated lenses of water-saturated sediments in the shallow subsurface. The electrical resistivity profiles orthogonal to the SMF (P2 and P3) show the presence of discontinuities within the second layer at locations farther away from the zones of mapped surface deformation (Profile P2 and P3, Figs 8a to d). We interpret these discontinuities as older, buried intrasedimentary faults, possibly associated with previous ruptures along the SMF. These buried faults possibly represent zones of paleoseismic deformation along the SMF.

### 5.3 Implications for seismic hazards

We observe that earthquake epicenter distribution across the Karonga area (Fig. 1) cover a broad zone, extending to the east and west of the location and trend of the SMF. We therefore suggest that the other buried normal faults in Karonga area, mapped in this study (Fig. 6; KPF, KTF and LF) are or could be seismically active. Previous studies have showed that some of the most devastating earthquake events in the world were associated with ruptures along previously-unidentified buried faults of all kinds. Examples include the 1886 $M_w$ 7.3 Charleston earthquake which ruptured a buried strike-slip-reverse fault and resulted in 60 fatalities and damage of 2,000 buildings in South Carolina, United States (Marple & Talwani, 2000; Durá-Gómez & Talwani, 2009); $M_s$ 6.9 1980 Irpinia, Italy earthquake which nucleated on a buried normal fault and resulted in 2,483 fatalities, 7,700 injuries, and left 250,000 homeless (Pantosti *et al.* 1993; Rovida *et al.* 2011); $M_w$ 6.7 1994 Northridge earthquake which ruptured a blind thrust fault and resulted in 57 fatalities, over

8,700 injuries and property damage worth billions of dollars in California, United States (Davis & Namson, 1994); and the $M_w$ 6.6 2003 Bam, Iran earthquake which ruptured a buried strike-slip fault, resulting in over 26,271 fatalities and up to 30,000 injuries (Fielding *et al*. 2009). This historical record therefore suggests that special attention be paid to SMF and other identified buried faults in Karonga area of Northern Malawi.

We observe that the lenses of water-saturated sediment along the SMF rupture zone (Figs 7a-b and 8c-d) are still preserved in the shallow-subsurface six years after the causative earthquake. We postulate that in the event of any future earthquakes, these preserved liquefied sediment sites are potential zones of ground failure (reliquefaction). The sites also represent mechanically weak zones that pose potential hazards to engineering structures built above them.

## 6 CONCLUSIONS

Our analyses and interpretation of aeromagnetic and electrical resistivity tomography along the Karonga area of Northern Malawi showed that the 2009 Karonga Earthquake is associated with the partial rupture of a pre-existing buried basement fault, called the St. Mary Fault. We suggest that unruptured segments of this fault constitute a high seismic hazard in the area. We present for the first time the seismotectonic setting of Karonga area of Northern Malawi, and aside from the SMF, we report on the presence, location and geometry of other possibly seismogenic buried faults in the area. We also show that areas underlain by preserved earthquake liquefaction-related structures in the shallow subsurface

will likely fail in the event of a future earthquake. Our electrical resistivity surveys reveal paleoseismic structures in the shallow-subsurface, and we propose trenching at these locations to investigate the detailed paleoseismic history of the SMF. Our study demonstrates that the integration of electrical resistivity tomography and aeromagnetic data can be very useful in seismic hazard analysis.

## ACKNOWLEDGEMENTS

This work was partially supported by the National Science Foundation (NSF) grant no. II – 1358150 and NSF-EAR 1255233. We thank the 2015 International Research Experience for Students (IRES) participants B. Clappe, C. Hull, T. Johnson, V. Nyalugwe, and S. Dawson for helping with the acquisition of the resistivity data. The aeromagnetic and resistivity data used in this study can be obtained from the Malawi Geological Survey. The resistivity data is also archived at the GeoPRISMS data portal. The Council for Geosciences, South Africa provided the old aeromagnetic data.

## REFERENCES

Aeromagnetic Map of Malawi, 1985. Malawi Geologic Survey Internal Report, Zomba, Malawi.

Ambraseys, N.N. & Adams, R.D., 1991. Reappraisal of major African earthquakes, south of 20°N, 1900–1930, *Nat. Hazards*, **4**(4)**,** 389–419.

Arkani-Hamed, J., 1988. Differential reduction-to-the-pole of regional magnetic anomalies, *Geophys.*, **53,** 1592–1600.

Baranov, V., 1957. A new method for interpretation of aeromagnetic maps: Pseudo-gravimetric anomalies, *Geophys.*, **22,** 359-383.

Biggs, J., Nissen, E., Craig, T., Jackson, J. & Robinson, D.P., 2010. Breaking up the hanging wall of a rift-border fault: the 2009 Karonga earthquakes, Malawi, *Geophys. Res. Lett.*, **37,** L11305.

Craig, T.J., Jackson, J.A., Priestley, K. & McKenzie, D., 2011. Earthquake distribution patterns in Africa: their relationship to variations in lithospheric and geological structure, and the rheological implications, *Geoph. J. Int.*, **185,** 403-434.

Davis, T.L. & Namson, J.S., 1994. A balanced cross section analysis of the 1994 Northridge earthquake and thrust fault seismic hazards in southern California, *Nature*, **372,** 167-169.

Durá-Gómez, I. & Talwani, P., 2009. Finding faults in the Charleston area, South Carolina: 1. Seismological data, *Seis. Res. Lett.*, **80**(5)**,** 883-900.

Ebinger, C.J., Deino, A.L., Tesha, A.L., Becker, T. & Ring, U., 1993. Tectonic controls on rift

basin morphology: evolution of the northern Malawi (Nyasa) rift, *J. of Geoph. Res.: Solid Earth*, **98**(B10)**,** 17821-17836.

Ebinger, C.J., Rosendahl, B. & Reynolds, D., 1987. Tectonic model of the Malawi rift, Africa, *Tectonophysics*, **141,** 215–235.

Fielding, E.J., Lundgren, P.R., Bürgmann, R. & Funning, G.J., 2009. Shallow fault-zone dilatancy recovery after the 2003 Bam earthquake in Iran, *Nature*, **458**(7234)**,** 64-68.

Goda, K., Gibson, E.D., Smith, H.R., Biggs, J. & Hodge, M., 2016. Seismic Risk Assessment of Urban and Rural Settlements around Lake Malawi, *Front. in Built Env.*, **2**, 30.

Hamiel, Y., Baer, G., Kalindekafe, L., Dombola, K. & Chindandali, P., 2012. Seismic and aseismic slip evolution and deformation associated with the 2009–2010 northern Malawi earthquake swarm, East African Rift, *Geophys. J. Int.*, **191,** 898–908.

Hodge, M., Biggs, J., Goda, K. & Aspinall, W., 2015. Assessing infrequent large earthquakes using geomorphology and geodesy: the Malawi Rift, *Nat. Hazards*, **76**(3)**,** 1781-1806.

Jackson, J.A. & Blenkinsop, T., 1997. The Bilila–Mtakataka faultinMalawi:anactive, 100-km long, normal fault segment in thick seismogenic crust, *Tectonics*, **16,** 137–150.

Kearey, P., Klepeis, K.A. & Vine, F.J., 2009. Global Tectonics, *3rd ed., Wiley-Blackwell, Oxford*.

Kolawole, F., Atekwana, E.A., Laó-Dávila, D.A., Abdelsalam, M.G., Ivey, T., Chindandali, P.R., Salima, J. & Kalindikafe, L., 2016. 2009 Karonga Earthquake associated with reactivation of structures within the Mugesse Shear Zone, Malawi: Evidence from aeromagnetic data, *American Geophysical Union (AGU) 2016 Fall meeting* Poster number **T51C-2933.**

Loke, M.H., 2001. Electrical imaging surveys for environmental and engineering studies, A practical guide to 2-D and 3-D surveys: RES2DINV Manual, *IRIS Instruments*.

Loke, M. & Barker, R., 1996. Rapid least inversion of apparent resistivity pseudosections using quasi Newton's method, *Geoph. Prosp.*, **44,** 131–152.

Macheyeki, A.S., Mdala, H., Chapola, L.S., Manhiça, V.J., Chisambi, J., Feitio, P., Ayele, A., Barongo, J., Ferdinand, R.W., Ogubazghi, G. & Goitom, B., 2015. Active fault mapping in Karonga-Malawi after the December 19, 2009 Ms 6.2 seismic event, *J. of Afr. Earth Sci.*, **102,** 233-246.

Marple, R.T. & Talwani, P., 2000. Evidence for a buried fault system in the Coastal Plain of the Carolinas and Virginia—Implications for neotectonics in the southeastern United States, *Geol. Soc. of Amer. Bull.*, **112**(2)**,** 200-220.

Mortimer, E., Paton, D.A., Scholz, C.A., Strecker, M.R. & Blisniuk, P., 2007. Orthogonal to oblique rifting: effect of rift basin orientation in the evolution of the North basin, Malawi Rift, East Africa, *Basin Res.*, **19**(3)**,** 393-407.

Oliva S.J.C., Ebinger, C.J., Keir, D., Shillington, D.J. & Chindandali, P.R.N., 2016. Deciphering the role of fluids in early stage rifting from full moment tensor inversion of East African earthquakes, *American Geophysical Union (AGU) 2016 Fall meeting* poster **T51C-2942**.

Pantosti, D., Schwartz, D.P. & Valensise, G., 1993. Paleoseismology along the 1980 surface rupture of the Irpinia fault: implications for earthquake recurrence in the southern Apennines, Italy, *J. of Geophys. Res.: Solid Earth*, **98**(B4)**,** 6561-6577.

Ring, U., 1994. The influence of preexisting structure on the evolution of Cenozoic Malawi Rift (East African Rift System), *Tectonics*, **13**(2)**,** 313-326.

Ring, U., Kröner, A., Buchwaldt, R., Toulkeridis, T. & Layer, P.W., 2002. Shear-zone patterns and eclogite-facies metamorphism in the Mozambique belt of northern Malawi, east-central Africa: implications for the assembly of Gondwana, *Precambrian Res.*, **116**(1)**,** 19-56.

Rovida, A., Camassi, R., Gasperini, P. & Stucchi, M., 2011. CPTI11, the 2011 version of the Parametric Catalogue of Italian Earthquakes, *Milano, Bologna*.

Saria, E., Calais, E., Stamps, D.S., Delvaux, D. & Hartnady, C.J.H., 2014. Present-day kinematics of the East African Rift, *J. Geoph. Res.*: *Solid Earth*, **119**(4)**,** 3584-3600.

Schrenk, F., Bromage, T.G., Betzler, C.G., Ring, U. & Juwayeyi, Y.M., 1993. Oldest Homo and Pliocene biogeography of the Malawi rift, *Nature*, **365,** 833-836.

Wheeler, W. & Karson, J., 1989. Structure and kinematics of the Livingstone Mountains border fault zone, Nyasa (Malawi) Rift, southwestern Tanzania, *J. Afric. Earth Sci. (and Mid. East)*, **8,** 393–413.

VITA

Folarin Kolawole

Candidate for the Degree of

Master of Science

Thesis: $M_W$ 6.0 KARONGA, MALAWI EARTHQUAKE OCCURRED ON CENOZOIC FAULTS THAT REACTIVATED PRECAMBRIAN SHEAR ZONE: EVIDENCE FROM AEROMAGNETIC AND ELECTRICAL RESISTIVITY IMAGING

Major Field: Geology

Biographical:

Education:

Completed the requirements for the Master of Science degree in Geology at Oklahoma State University, Stillwater, Oklahoma in July, 2017.

Completed the requirements for the Bachelor of Science degree in Geology at Federal University of Technology, Akure (F.U.T.A.), Nigeria, West Africa, in October, 2008.

Experience:

- Geomarine Systems Limited, Port Harcourt, Nigeria
- Chinese National Petroleum Corporation (BGP-CNPC), Port Harcourt, Nigeria
- Nigeria National Petroleum Corporation, NAPIMS JV Op., Lagos, Nigeria

Professional Memberships:

American Association of Petroleum Geologists (AAPG)
Geological Society of America (GSA)
Society of Exploration Geophysicists (SEG)
National Association of Black Geoscientists (NABG)
American Geophysical Union (AGU)

ADVISER'S APPROVAL: Dr. Estella Atekwana